The Astrophysical Journal, 978:56 (22pp), 2025 January 01 https://doi.org/10.3847/1538-4357/ad93a9

Long Plateau Doth So: How Internal Heating Sources Affect Hydrogen-rich Supernova Light Curves

Tatsuya Matsumoto[1,2,3], Brian D. Metzger[1,4], and Jared A. Goldberg[4]
[1] Department of Physics and Columbia Astrophysics Laboratory, Columbia University, Pupin Hall, New York, NY 10027, USA
[2] Department of Astronomy, Kyoto University, Kitashirakawa-Oiwake-cho, Sakyo-ku, Kyoto, 606-8502, Japan
[3] Hakubi Center, Kyoto University, Yoshida-honmachi, Sakyo-ku, Kyoto, 606-8501, Japan
[4] Center for Computational Astrophysics, Flatiron Institute, 162 5th Ave, New York, NY 10010, USA
Received 2024 January 24; revised 2024 November 14; accepted 2024 November 15; published 2024 December 24

Abstract

Some hydrogen-rich core-collapse supernovae (SNeIIP) exhibit evidence of a sustained energy source powering their light curves, resulting in a brighter and/or longer-lasting hydrogen recombination plateau phase. We present a semi-analytic SNIIP light-curve model that accounts for the effects of an arbitrary internal heating source, considering as special cases ^{56}Ni/^{56}Co decay, a central engine (magnetar or accreting compact object), and shock interaction with a dense circumstellar disk. While a sustained internal power source can boost the plateau luminosity commensurate with the magnitude of the power, the duration of the recombination plateau can typically be increased by at most a factor of ∼2–3 compared to the zero-heating case. For a given ejecta mass and initial kinetic energy, the longest plateau duration is achieved for a constant heating rate at the highest magnitude that does not appreciably accelerate the ejecta. This finding has implications for the minimum ejecta mass required to explain particularly long-lasting SNe, such as iPTF14hls, and for confidently identifying rare explosions of the most massive hydrogen-rich (e.g., Population III) stars. We present a number of analytic estimates that elucidate the key features of the detailed model.

Unified Astronomy Thesaurus concepts: Type II supernovae (1731)

1. Introduction

Roughly 75% of all stellar explosions are core-collapse supernovae (SNe; e.g., F. Mannucci et al. 2007), of which ≈70% are hydrogen-rich, i.e., Type II SNe (e.g., D. A. Perley et al. 2020). Roughly three-quarters of the Type II SNe are further of the IIP class (SNeIIP), with a plateau-shaped light-curve phase lasting typically around 100 days (R. Barbon et al. 1979; J. P. Anderson et al. 2014; T. Faran et al. 2014; S. Valenti et al. 2016; L. Martinez et al. 2022a). In most cases, the luminosity during the plateau phase is supported mainly by the thermal energy deposited by the SN shock, its evolution dictated by a cooling and recombination wave receding inward through the expanding envelope (E. K. Grassberg et al. 1971; E. K. Grasberg & D. K. Nadezhin 1976; S. W. Falk & W. D. Arnett 1977; I. I. Litvinova & D. K. Nadezhin 1983; I. Y. Litvinova & D. K. Nadezhin 1985; N. N. Chugai 1991; D. V. Popov 1993; T. Faran et al. 2019).

The properties of SNIIP light curves, such as the duration and luminosity of the plateau phase, can along with spectral information such as photospheric velocities be used to constrain the ejecta properties (e.g., O. Pejcha & J. L. Prieto 2015; L. Martinez et al. 2022b), though with substantial degeneracies (e.g., L. Dessart & D. J. Hillier 2019; J. A. Goldberg et al. 2019). These constraints frequently make use of analytic scaling relations calibrated to numerical simulations (e.g., D. V. Popov 1993; S. Zha et al. 2023). It is also known that the sustained heating from the ^{56}Ni→^{56}Co→^{56}Fe decay chain acts to flatten and extend the duration of the plateau (e.g., T. R. Young 2004; D. Kasen & S. E. Woosley 2009; M. C. Bersten et al. 2011; E. Nakar et al. 2016; T. Sukhbold et al. 2016; J. A. Goldberg et al. 2019; A. Kozyreva et al. 2019), which can also be included in numerically calibrated analytic estimates.

However, there is increasing evidence for the need for extra energy sources beyond ^{56}Ni in a growing subset of SNe, the most extreme cases being superluminous SNe (SLSNeII; A. Gal-Yam 2019; C. Inserra 2019). This "extra" heating source has variously been attributed to circumstellar medium (CSM) interaction (e.g., A. Fassia et al. 2000; N. Smith & R. McCray 2007; A. A. Miller et al. 2009; E. Chatzopoulos et al. 2012; C. Inserra et al. 2012; J. C. Mauerhan et al. 2013; C. Fransson et al. 2014; N. Smith et al. 2014; K. A. Bostroem et al. 2019; A. Nyholm et al. 2020; see also M. Fraser 2020 for a review), the injection of rotational energy from a rapidly spinning magnetized neutron star (D. Kasen & L. Bildsten 2010; S. E. Woosley 2010; T. Sukhbold & T. A. Thompson 2017; L. Dessart 2018), or accretion energy from a black hole (J. Dexter & D. Kasen 2013; R. Perna et al. 2018) or neutron star (B. D. Metzger et al. 2018). An extreme example is iPTF14hls, which produced a plateau-like (optically thick) phase lasting for ∼1000 days (I. Arcavi et al. 2017; J. Sollerman et al. 2019), only finally to reveal the appearance of narrow emission lines and hence the presence of CSM interaction (J. E. Andrews & N. Smith 2018).

Extremely luminous or long-lasting SNeIIP can also result from rare or exotic explosions of extremely massive progenitors, such as pair-instability SNe (PISNe), from stars of $\gtrsim 100 M_{\odot}$ (G. Rakavy & G. Shaviv 1967; A. Heger & S. E. Woosley 2002; S. E. Woosley et al. 2007; K.-J. Chen et al. 2023). However, the standard analytic expressions commonly used to estimate the ejecta properties from observables like plateau duration and luminosity (e.g., D. V. Popov 1993; T. Sukhbold et al. 2016), and hence to identify such rare explosion classes, in general do not apply in

the presence of additional heating sources. This motivates the present study to explore the full landscape of theoretically permitted SNIIP properties, allowing for an arbitrary heating source evolution, in order to ascertain what robust constraints can be placed by SN observations on the stellar progenitor properties (particularly the ejecta mass). Such a framework would help address whether exceptionally long-duration light curves like iPTF14hls necessitate an atypically massive stellar progenitor or whether an otherwise ordinary-mass explosion with a powerful internal heating source (e.g., from CSM interaction) is alone sufficient.

The Vera C. Rubin Observatory (Rubin; Ž. Ivezić et al. 2019) will monitor roughly half of the extragalactic sky over 10 yr, during which it is expected to observe millions of SNeIIP (LSST Science Collaboration 2009). This unprecedented sample will enable detailed studies of the distribution of explosion properties (e.g., J. W. Murphy et al. 2019; J. A. Goldberg & L. Bildsten 2020; L. Martinez et al. 2022a) and how they map onto progenitor star (e.g., N. L. Strotjohann et al. 2024) and host galaxy properties (e.g., A. Gagliano et al. 2023). In addition to the many relatively nearby SNe observed by Rubin, rare explosions arising from the first generations of stars (e.g., Population III) are targets for high-redshift surveys such as Euclid (e.g., T. J. Moriya et al. 2022) and the Nancy Grace Roman Space Telescope (e.g., B. M. Rose et al. 2021). The analytic estimates derived in this paper will be usefully applied to constrain the ejecta properties or energy sources for future large samples of SNeIIP or for obtaining robust conclusions for individual exceptional events like iPTF14hls.

This paper is organized as follows. In Section 2, we generalize existing semi-analytic SNIIP light-curve models to include the presence of an arbitrary internal heating source. In Section 3, we first consider the case of a temporally constant heating source, providing ample analytic estimates that help interpret our numerical results. In Section 4, we expand our considerations to the case of a broken-power-law heating rate, which we show approximates the behavior of most physical heating sources, ranging from radioactive ^{56}Ni decay to a central magnetar or accreting engine to CSM interaction. In Section 5, we discuss the implications of our results, and in Section 6, we summarize our findings and conclude. Readers who are not interested in analytical derivations can go directly to Section 5 and Figure 12, where our main findings and their implications are discussed.

2. Generalized Popov Model

We generalize the D. V. Popov (1993) model to include a central heating source of arbitrary magnitude, which will in essence act to lengthen the optically thick photospheric phase, i.e., the "plateau" phase (at least for nonextremal heating rates). While the "plateau" should be defined by the phase over which the light curve has a flat shape as identified in observations, defining it in a formal way is not straightforward (see, e.g., T. Sukhbold et al. 2016; J. A. Goldberg et al. 2019 for several definitions in numerical studies). Physically, there are two important timescales: one is the diffusion time at which the most photons diffuse out of ejecta; the other is the time when the ejecta becomes optically thin—that is, the end (start) of the photospheric (nebular) phase. During the nebular phase, thermal emission is no longer necessarily produced. As we will see below, under weak energy injection, the light curve drops at the diffusion time and traces the injection luminosity onward. For strong injection, the light curve never experiences a drop and smoothly enters the nebular phase. Since our interest is in obtaining the maximum duration of the plateau under energy injection, we define the plateau phase as the duration over which the ejecta shell is still opaque to electron scattering as the "plateau," even when the light curve is not flat. This serves as a conservative upper limit on the plateau duration.

Prior to when the ejecta cools sufficiently for hydrogen recombination to set in, its evolution follows the well-known Arnett model (W. D. Arnett 1980, 1982) with an additional heating source (e.g., D. Kasen & L. Bildsten 2010; E. Chatzopoulos et al. 2012; B. D. Metzger et al. 2015). The first law of thermodynamics is applied to a one-zone model:[5]

$$\frac{dE}{dt} = -P\frac{dV}{dt} - L + H, \tag{1}$$

where E, P, $V = \frac{4\pi}{3}R^3$, R, L, and H are the internal thermal energy, pressure, volume, radius, radiated luminosity, and (specified) heating rate, respectively. We assume that radiation pressure dominates over gas pressure, such that $E = aT^4V$ and $P = E/(3V)$, respectively, where a is the radiation constant and T is the internal temperature. The radiated luminosity follows from the diffusion approximation:

$$L \simeq 4\pi R^2 \frac{c}{3\kappa\rho}\frac{d(aT^4)}{dR} \sim \frac{t_{\rm dyn}E}{t_{\rm diff}^2}, \tag{2}$$

where the dynamical and diffusion timescales are, respectively, defined by

$$t_{\rm dyn} \equiv \frac{R}{v}, \tag{3}$$

$$t_{\rm diff} \equiv \left(\frac{3\kappa M}{4\pi c v}\right)^{1/2} \simeq 110\ {\rm day}\ M_{10}^{1/2} v_{6000}^{-1/2}. \tag{4}$$

Here, $\kappa = 0.34\ {\rm cm^2\ g^{-1}}$ is the Thomson opacity for fully ionized solar composition material, c is the speed of light, and we have introduced the shorthand notation $M = 10M_{10}\,M_\odot$ and $v = 6000v_{6000}\,{\rm km\ s^{-1}}$ for the ejecta mass and characteristic velocity, respectively. Equation (1) can now be written as

$$\frac{dE}{dt} = -\frac{E}{t_{\rm dyn}} - \frac{t_{\rm dyn}E}{t_{\rm diff}^2} + H. \tag{5}$$

The first term in Equation (1) accounts for the loss of internal energy due to PdV work done on the ejecta by itself. This term acts to increase the ejecta kinetic energy $E_{\rm kin}$, according to

$$\frac{dE_{\rm kin}}{dt} = P\frac{dV}{dt}. \tag{6}$$

For homologously expanding ejecta of assumed constant density, $\rho = M/V$, and velocity $v' = v(r/R)$, we have

$$E_{\rm kin} = \int_0^R \left(\frac{1}{2}\rho v'^2\right)4\pi r^2 dr = \frac{3}{10}Mv^2 \simeq 2.2\times 10^{51}\ {\rm erg}\ M_{10}v_{6000}^2. \tag{7}$$

[5] The original models of W. D. Arnett (1980, 1982) and D. V. Popov (1993) employ a radial temperature profile corresponding to a solution to the diffusion equation. The simpler one-zone model adopted in this paper nevertheless reproduces the normalization and parameter scalings of these original models, motivating our approach. We also discuss the validation of the one-zone approximation in more detail in Appendix A.

Note that we have neglected any contribution to $E_{\rm kin}$ from a high-velocity tail $v' \gg v$, which contributes to the early-time shock cooling emission but not to the plateau. Equation (6) thus becomes

$$M\frac{dv}{dt} = \frac{20\pi}{3}R^2P. \tag{8}$$

Equations (5) and (8) determine the time evolution of ejecta until the hydrogen recombination phase begins.

The recombination phase starts when the effective temperature of the photosphere decreases to the hydrogen recombination temperature, $T_{\rm i} \simeq 6000$ K. The photosphere temperature is defined as

$$T_{\rm eff} \equiv \left(\frac{L}{4\pi\sigma_{\rm SB}R^2}\right)^{1/4} \simeq 1.1\frac{T}{\tau^{1/4}}, \tag{9}$$

where $\sigma_{\rm SB}$ is the Stefan–Boltzmann constant, $\tau = \kappa R\rho$ is the Thompson optical depth through the ejecta (i.e., assuming it is fully ionized), and the second equality makes use of Equation (2).

After recombination begins at $t = t_{\rm i}$, a sharp recombination front forms and begins to recede back through the ejecta shell. Outside this front, the ejecta is neutral and transparent to radiation. Therefore, we regard the photosphere radius $R_{\rm ph}$ as coinciding with the recombination front, at the dimensionless coordinate $x \equiv R_{\rm ph}/R \leqslant 1$. We retain a one-zone model similar to that described earlier to calculate the evolution of the fully ionized region (within the photosphere) during the recombination phase. All quantities retain the same meaning, except the ejecta radius R is now replaced with $R_{\rm ph} = xR$. For instance, the volume of the ionized region becomes $V = \frac{4\pi}{3}(xR)^3$, while the radiated luminosity becomes

$$L \simeq 4\pi(xR)^2\frac{c}{3\kappa\rho}\frac{aT^4}{xR} = \frac{t_{\rm dyn}E}{x^2t_{\rm diff}^2}. \tag{10}$$

Equating this to the photosphere luminosity, $L = 4\pi(xR)^2\sigma_{\rm SB}T_{\rm i}^4$, gives an expression analogous to Equation (9) but with the replacements $T_{\rm eff} \to T_{\rm i}$ and $\tau \to x\tau$. Combined with Equation (5), this gives the evolution of the recombination depth (J. Dexter & D. Kasen 2013):

$$\frac{dx}{dt} = -\frac{2x}{5t_{\rm dyn}} - \frac{t_{\rm dyn}}{5t_{\rm diff}^2x} + \frac{H}{5H_{\rm cr}}\frac{1}{t_{\rm dyn}x^3}, \tag{11}$$

where we have defined

$$H_{\rm cr} = 4\pi(vt_{\rm diff})^2\sigma_{\rm SB}T_{\rm i}^4 \tag{12}$$

$$\simeq 3.0 \times 10^{43}\,{\rm erg\,s^{-1}}\,M_1v_{6000}T_{\rm i,6000}^4$$

and $T_{\rm i} = 6000T_{\rm i,6000}$ K. This critical heating rate controls the recombination time and will be used in the analytic estimates below.

We have neglected the acceleration of the ejecta during the recombination phase. This is usually justified because the acceleration timescale at recombination ($t \simeq t_{\rm i}$),

$$\frac{v}{dv/dt}|_{t_{\rm i}} = \frac{v}{\frac{5}{4}\kappa aT_{\rm i}^4} \simeq 1700\ {\rm day}\ v_{6000}T_{\rm i,6000}^{-4}, \tag{13}$$

greatly exceeds the dynamical timescale,[6] where we have used Equations (8) and (9) and set $T_{\rm eff} = T_{\rm i}$. Acceleration also becomes negligible after radiation begins to diffuse out of the ejecta ($t \gtrsim t_{\rm diff}$), due to the associated loss of thermal pressure.

In the following sections, we solve the above equations for different central heating sources $H(t)$ and ejecta properties. The latter include the total mass M, initial size (usually, the progenitor star radius) R_0, initial internal energy E_0, and initial kinetic energy $E_{\rm kin,0}$.[7] Throughout, we assume solar abundances and $\kappa = 0.34\,{\rm cm^2\,g^{-1}}$ (though this could readily be generalized to different abundances by modifying μ and κ accordingly). We also assume that the ejecta internal and kinetic energies are initially comparable, $E_0 \simeq E_{\rm kin,0}$ at $t = 0$, with the total explosion energy equal to their sum. After just a few dynamical times, most of the initial internal energy is converted into kinetic energy by PdV work, causing the ejecta to reach a terminal speed $v = \sqrt{2}\,v_0$, where v_0 is the initial velocity calculated from $E_{\rm kin,0}$ and M (Equation (7)). For $E_{\rm kin,0} = 10^{51}$ erg and $M = 10M_\odot$, this gives $v_0 \simeq 4100\,{\rm km\,s^{-1}}$ and $v \simeq 5800\,{\rm km\,s^{-1}}$. Except where noted (e.g., Section 3.2), we hereafter express analytic estimates in terms of the terminal speed, v.

Before describing our results for specific heating sources, we review the original Popov estimates (D. V. Popov 1993; J. Dexter & D. Kasen 2013; T. Matsumoto et al. 2016), which are obtained by neglecting any heating or acceleration of the ejecta after the initial explosion. As shown below (around Equation (28)), the recombination phase begins on the timescale

$$t_{\rm i} \simeq 19\ {\rm day}\ E_{0,51}^{1/2}M_{10}^{-1/2}R_{0,500}^{1/2}v_{6000}^{-1}T_{\rm i,6000}^{-2}, \tag{15}$$

where $E_0 = 10^{51}E_{0,51}$ erg, $R_0 = 500R_{0,500}\,R_\odot$, and we have implicitly assumed $t_{\rm i} \ll t_{\rm diff}$. Under these assumptions, Equation (11) has the following analytic solution:

$$x = \left(\frac{t}{t_{\rm i}}\right)^{-\frac{2}{5}}\left[1 + \frac{1}{7}\left(\frac{t_{\rm i}}{t_{\rm diff}}\right)^2 - \frac{1}{7}\left(\frac{t_{\rm i}}{t_{\rm diff}}\right)^2\left(\frac{t}{t_{\rm i}}\right)^{\frac{14}{5}}\right]^{\frac{1}{2}}. \tag{16}$$

The plateau duration corresponds to when the ejecta fully recombines ($x(t_{\rm pl,Popov}) = 0$), giving

$$t_{\rm pl,Popov} = t_{\rm i}\left[1 + 7\left(\frac{t_{\rm diff}}{t_{\rm i}}\right)^2\right]^{5/14} \simeq 7^{5/14}t_{\rm i}^{2/7}t_{\rm diff}^{5/7} \tag{17}$$

$$\simeq 130\ {\rm day}\ E_{0,51}^{1/7}M_{10}^{3/14}R_{0,500}^{1/7}v_{6000}^{-9/14}T_{\rm i,6000}^{-4/7},$$

where the second equality on the first line assumes $t_{\rm i} \ll t_{\rm diff}$. At the same level of approximation, the total radiated energy and

[6] This may break down for low-velocity events such as SN precursors (e.g., N. L. Strotjohann et al. 2021; T. Matsumoto & B. D. Metzger 2022a). See D. Tsuna et al. (2024) for an attempt to include the acceleration during the recombination phase.

[7] Radiation pressure dominates over gas pressure for large explosion energies, obeying

$$E_0 \gtrsim 1.3 \times 10^{48}\,{\rm erg}\,(\mu/0.60)^{-1}M_{10}^{4/3}R_{0,500}^{-1}, \tag{14}$$

where μ is the mean molecular weight.

average plateau luminosity are given, respectively, by

$$E_{\rm pl} = \int_{t_{\rm i}}^{t_{\rm pl}} L dt \simeq \frac{56\pi}{55}\sigma_{\rm SB} T_{\rm i}^4 v^2 t_{\rm i}^3 \left(\frac{t_{\rm i}}{7^{\frac{1}{2}} t_{\rm diff}}\right)^{-\frac{11}{7}}, \quad (18)$$

$$\simeq 2.8 \times 10^{49}\,{\rm erg}\, E_{0,51}^{5/7} M_{10}^{1/14} R_{0,500}^{5/7} v_{6000}^{-3/14} T_{\rm i,6000}^{8/7},$$

$$L_{\rm pl} \equiv \frac{E_{\rm pl}}{t_{\rm pl}} \simeq \frac{7^{3/7}56}{55}\pi\sigma_{\rm SB} T_{\rm i}^4 v^2 t_{\rm i}^{8/7} t_{\rm diff}^{6/7} \quad (19)$$

$$\simeq 2.4 \times 10^{42}\,{\rm erg\,s^{-1}}\, E_{0,51}^{4/7} M_{10}^{-1/7} R_{0,500}^{4/7} v_{6000}^{3/7} T_{\rm i,6000}^{12/7},$$

where we have used $t_{\rm pl,Popov}$ for $t_{\rm pl}$. These expressions exhibit slightly different exponents and normalization from those originally derived by D. V. Popov (1993), who assumed a self-similar radial temperature profile, which is not necessarily achieved (e.g., D. K. Khatami & D. N. Kasen 2019). These expressions have been compared with the results of radiation hydrodynamic simulations (D. Kasen & S. E. Woosley 2009; T. Sukhbold et al. 2016; J. A. Goldberg et al. 2019), their accuracy being confirmed to within a factor of a few.[8]

3. Constant Heating Rate

We now solve the equations presented in the previous section to explore how the SN plateau phase is modified by a temporally constant heating source of arbitrary magnitude. While a constant heating rate only represents a crude approximation to a more physical time-evolving power source, this simple assumption enables us to obtain general physical insights into the impact of heating and to derive useful analytical formulae. Furthermore, we show later that the constant-heating case bounds the light-curve behavior for more complex, physically motivated heating curves, in particular by defining the maximal plateau duration.

A given model is specified by the (constant) heating rate H and the initial conditions of the explosion, as mentioned above. At early times ($t < t_{\rm i}$), the effective temperature exceeds the recombination value ($T_{\rm eff} > T_{\rm i}$), and we solve Equations (5) and (8) until $T_{\rm eff} = T_{\rm i}$ at $t_{\rm i}$. During the recombination phase, we solve Equation (11) for $x(t)$. The evolution is followed until the nebular phase, which we define as when the optical depth decreases to unity: $x\tau = 1$.

Figure 1 depicts the time evolution of the effective temperature, luminosity, and dimensionless photospheric radius for various values of the heating rate $H = 10^{40}$–$10^{46}\,{\rm erg\,s^{-1}}$, adopting ejecta properties of $M = 10\,M_\odot$, $R_0 = 500\,R_\odot$, and $E_0 = E_{\rm kin,0} = 10^{51}$ erg (corresponding to $v_0 \simeq 4100\,{\rm km\,s^{-1}}$ and $v \simeq 5800\,{\rm km\,s^{-1}}$), typical of Type II SNe (e.g., D. Kasen & S. E. Woosley 2009). The results are qualitatively summarized as follows. When the heating rate is sufficiently small ($H \lesssim 10^{41}\,{\rm erg\,s^{-1}}$), its effect is negligible and the result is indistinguishable from the zero-heating case $H = 0$.

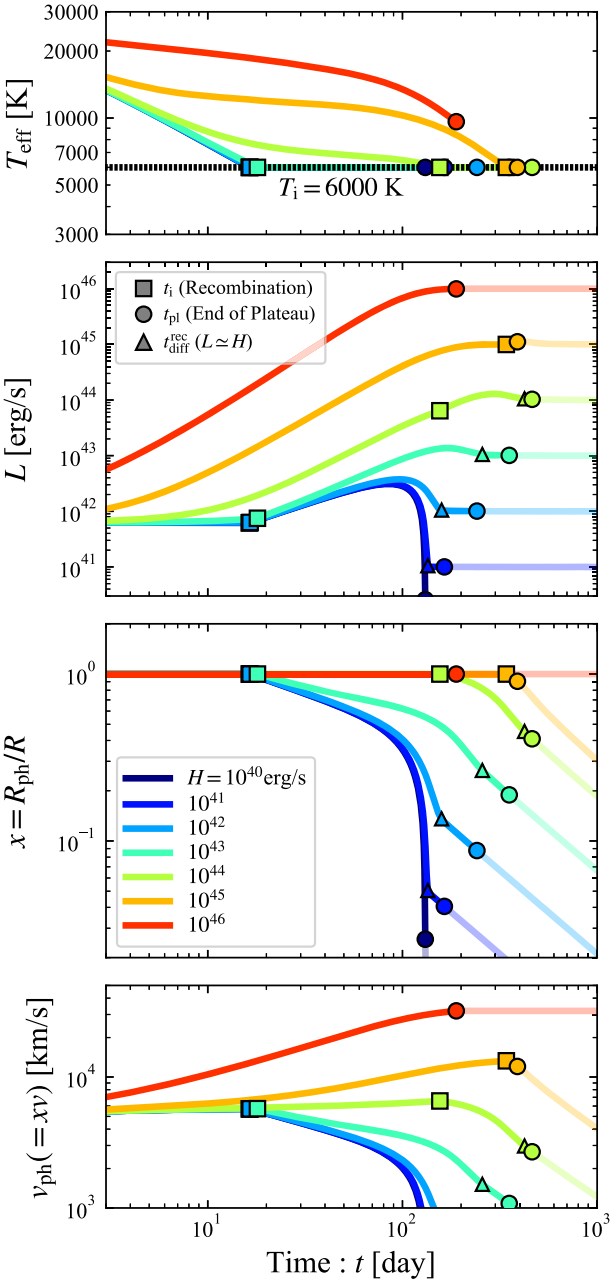

Figure 1. Time evolution of the effective temperature, bolometric luminosity, and location and velocity of the photosphere (from top to bottom) for different constant heating rates as marked. The recombination phase begins when $T_{\rm eff} = T_{\rm i}$ at $t_{\rm i}$ (marked as squares). The ejecta enters the nebular phase when the optical depth becomes smaller than unity at $t_{\rm pl}$ (marked as circles), providing one definition of the plateau duration. After time $t_{\rm diff}^{\rm rec}$ (marked as triangles) during the recombination phase, the luminosity starts to track the internal heating rate, a transition that may also be observationally associated with the end of the plateau. The adopted ejecta parameters are $M = 10\,M_\odot$, $R_0 = 500\,R_\odot$, $E_0 = E_{\rm kin,0} = 10^{51}$ erg ($v_0 \simeq 4100\,{\rm km\,s^{-1}}$).

As the heating rate increases, the plateau duration (equivalently, in our formulation, the beginning of the nebular phase) becomes longer but the initial onset $t_{\rm i}$ of the recombination phase remains largely unchanged up to $H \lesssim H_{\rm cr} \simeq 3 \times 10^{43}\,{\rm erg\,s^{-1}}$. The recombination time grows substantially for $H \gtrsim H_{\rm cr}$. For yet larger heating rates $H \gg H_{\rm cr}$, the recombination phase terminates earlier and the plateau duration shrinks, because the ejecta is now significantly accelerated by PdV work. The plateau duration thus achieves its maximal value for

[8] Numerical results in previous works can be summarized as

$$L_{50} = \tilde{L}_{50}\,{\rm erg\,s^{-1}}\, E_{\rm SN,51}^{5/6} M_{10}^{-1/2} R_{0,500}^{2/3}, \quad (20)$$

$$t_{\rm pl} = \tilde{t}_{\rm pl}\,{\rm day}\, E_{\rm SN,51}^{-1/6} M_{10}^{1/2} R_{0,500}^{1/6}, \quad (21)$$

where L_{50} is the bolometric luminosity at 50 days after the explosion and $E_{\rm SN} = 10^{51} E_{\rm SN,51}$ erg is the total explosion energy. D. Kasen & S. E. Woosley (2009) obtained $\tilde{L}_{50} \simeq 1.3 \times 10^{42}$ and $\tilde{t}_{\rm pl} \simeq 122$ with a different dependence of $t_{\rm pl} \propto E_{\rm SN,51}^{-1/4}$; T. Sukhbold et al. (2016) found $\tilde{L}_{50} \simeq 1.8 \times 10^{42}$ and $\tilde{t}_{\rm pl} \simeq 96$; and J. A. Goldberg et al. (2019) found $\tilde{L}_{50} \simeq 1.4 \times 10^{42}$ and a slightly different scaling (see their Equation (8)).

a given ejecta mass/explosion energy at the maximum heating rate that does not appreciably impact the ejecta dynamics ($H \simeq 10^{44}\,\mathrm{erg\,s^{-1}}$, for the adopted parameters). In the following, we derive analytical formulae for these timescales and the critical heating rates that delineate these regimes.

3.1. Without Acceleration

We first consider cases in which *PdV* acceleration is negligible following the initial dynamical timescale; this greatly simplifies the analysis and is a good approximation for small heating rates. For constant velocity, the dynamical timescale is identical to the time since explosion, $t_{\rm dyn} = t$ (or equivalently $R = vt$), and Equation (5) can be integrated to obtain

$$E = E_0\left(\frac{t_0}{t}\right)e^{-\frac{t^2-t_0^2}{2t_{\rm diff}^2}}\left[1 + \frac{t_{\rm diff}^2 H}{t_0 E_0}\left(e^{\frac{t^2-t_0^2}{2t_{\rm diff}^2}} - 1\right)\right], \tag{22}$$

where

$$t_0 = \frac{R_0}{v_0} \simeq 0.95\ \mathrm{day}\ R_{0,500}\, v_{6000}^{-1} \tag{23}$$

is the initial dynamical/expansion timescale and we again relate the initial and terminal ejecta speed, $v_0 = v/\sqrt{2}$. The second term within square brackets in Equation (22) represents the effect of the heating source. For typical SN ejecta properties, the diffusion time exceeds the initial expansion timescale, $t_{\rm diff} \gg t_0$; since initially the heating does not impact the ejecta evolution, the internal energy declines adiabatically, $E \propto t^{-1}$. This evolution is modified once the deposited energy becomes comparable to the internal energy, $tH \simeq t_0 E_0/t$. This occurs on the timescale

$$t_{\rm h} = \left(\frac{t_0 E_0}{H}\right)^{1/2} \simeq 33\ \mathrm{day}\ E_{0,51}^{1/2} R_{0,500}^{1/2} v_{6000}^{-1/2} H_{43}^{-1/2}, \tag{24}$$

where $H = 10^x H_x\,\mathrm{erg\,s^{-1}}$. When this timescale is shorter than the diffusion timescale, which is true for large heating rates,

$$H \gtrsim \frac{t_0 E_0}{t_{\rm diff}^2} \simeq 9.1 \times 10^{41}\,\mathrm{erg\,s^{-1}}\, E_{0,51} M_{10}^{-1} R_{0,500}, \tag{25}$$

the time evolution of the internal energy can be summarized as

$$E \simeq \begin{cases} \dfrac{t_0 E_0}{t} & : t < t_{\rm h}, \\ tH & : t_{\rm h} < t < t_{\rm diff}, \\ \dfrac{t_{\rm diff}^2 H}{t} & : t_{\rm diff} < t. \end{cases} \tag{26}$$

When $t_{\rm h} > t_{\rm diff}$, the middle regime disappears.

The effective temperature evolves following Equation (9):

$$T_{\rm eff} \simeq T_{\rm i}\left(\frac{H}{H_{\rm cr}}\right)^{1/4} \begin{cases} \left(\dfrac{t}{t_{\rm h}}\right)^{-1/2} & : t < t_{\rm h}, \\ 1 & : t_{\rm h} < t < t_{\rm diff}, \\ \left(\dfrac{t}{t_{\rm diff}}\right)^{-1/2} & : t_{\rm diff} < t, \end{cases} \tag{27}$$

where $H_{\rm cr}$ is the critical heating rate introduced earlier (Equation (12)). The recombination time $t_{\rm i}$ is obtained by setting $T_{\rm eff} = T_{\rm i}$ with Equation (27). Noting that the effective temperature is constant for $t_{\rm h} < t < t_{\rm diff}$, we obtain

$$t_{\rm i} = \begin{cases} \left(\dfrac{t_0 E_0}{H_{\rm cr}}\right)^{1/2} & : H \leqslant H_{\rm cr}, \\ \left(\dfrac{t_{\rm diff}^2 H}{H_{\rm cr}}\right)^{1/2} & : H_{\rm cr} < H, \end{cases} \tag{28}$$

$$\simeq \begin{cases} 19\ \mathrm{day}\ E_{0,51}^{1/2} M_{10}^{-1/2} R_{0,500}^{1/2} v_{6000}^{-1} T_{\rm i,6000}^{-2} & : H \leqslant H_{\rm cr}, \\ 66\ \mathrm{day}\ v_{6000}^{-1} T_{\rm i,6000}^{-2} H_{43}^{1/2} & : H_{\rm cr} < H. \end{cases}$$

This timescale for $H < H_{\rm cr}$ is notably identical to that in the $H = 0$ limit (Equation (15)). Interestingly, the recombination time is discontinuous at $H = H_{\rm cr}$, because of the static effective temperature for $t_{\rm h} < t < t_{\rm diff}$, thus accounting for the sudden jump in the recombination time above $H \simeq H_{\rm cr} \simeq 3 \times 10^{43}\,\mathrm{erg\,s^{-1}}$.

For the recombination phase, while Equation (11) cannot be solved analytically for $H \neq 0$, the behavior of the solution can still be understood quantitatively. The three terms on the right-hand side of Equation (11) correspond to adiabatic cooling, radiative cooling (photon diffusion), and heating, respectively. First consider the limit of weak heating $H < H_{\rm cr}$. In such cases, just after the recombination starts, neither heating nor radiative losses are important, and the photosphere thus shrinks in time as $x \simeq (t/t_{\rm i})^{-2/5}$, corresponding to adiabatic evolution (Equation (16)). However, as x decreases, radiative cooling and heating eventually come to compete with or balance, respectively, the adiabatic cooling. For parameter regimes in which radiative cooling is subdominant, adiabatic cooling balances heating. This balance is achieved on the timescale

$$t_{\rm h}^{\rm rec} = \left(\frac{2H_{\rm cr}}{H}\right)^{5/8} t_{\rm i} \tag{29}$$

$$\simeq 59\ \mathrm{day}\ E_{0,51}^{1/2} M_{10}^{1/8} R_{0,500}^{1/2} v_{6000}^{-3/8} T_{\rm i,6000}^{1/2} H_{43}^{-5/8}.$$

At times $t > t_{\rm h}^{\rm rec}$, the photosphere stalls at $x \simeq (H/2H_{\rm cr})^{1/4}$ until radiative cooling takes over from adiabatic cooling in balancing heating. This occurs after, on the timescale

$$t_{\rm diff}^{\rm rec} = \left(\frac{2H}{H_{\rm cr}}\right)^{1/4} t_{\rm diff} \simeq 99\ \mathrm{day}\ M_{10}^{1/4} v_{6000}^{-3/4} T_{\rm i,6000}^{-2} H_{43}^{1/4}. \tag{30}$$

After this transition $t > t_{\rm diff}^{\rm rec}$, the photosphere continues to shrink again, this time as $x \simeq (H/H_{\rm cr})^{1/2} t_{\rm diff}/t$. In summary, for $H < H_{\rm cr}$ and $t_{\rm i} < t_{\rm h} < t_{\rm diff}$, the photosphere location evolves as

$$x \simeq \begin{cases} \left(\dfrac{t}{t_{\rm i}}\right)^{-2/5} & : t < t_{\rm h}^{\rm rec}, \\ \left(\dfrac{H}{2H_{\rm cr}}\right)^{1/4} & : t_{\rm h}^{\rm rec} < t < t_{\rm diff}^{\rm rec}, \\ \left(\dfrac{H}{H_{\rm cr}}\right)^{1/2} \dfrac{t_{\rm diff}}{t} & : t_{\rm diff}^{\rm rec} < t. \end{cases} \tag{31}$$

The superscripts "rec" in Equations (29) and (30) denote the heating and diffusion timescales during the recombination phase, respectively. After the diffusion timescale, the escaping luminosity roughly tracks the heating rate $L \simeq H$, as illustrated

by the triangles in Figure 1. While we have defined the end of the plateau as when the ejecta becomes optically thin, one could instead define this by the change in light-curve shape near $t_{\rm diff}^{\rm rec}$ (e.g., the location of the triangles for the $H = 10^{41}$ and 10^{42} erg s^{-1} cases in Figure 1). We discuss later in this section how our results change if we instead identify $t_{\rm diff}^{\rm rec}$ as the plateau duration.

For the opposite regime, radiative cooling dominates adiabatic cooling even before either balances heating. In these cases, the photosphere evolution follows Equation (16) until heating balances cooling at $t \simeq t_{\rm pl,Popov}$, after which x decreases following the final case in Equation (31). Such an evolutionary sequence is realized for low heating rates, below a critical value,

$$H \lesssim 0.66\left(\frac{t_{\rm i}}{t_{\rm diff}}\right)^{8/7} H_{\rm cr} \simeq 2.7 \times 10^{42}\ {\rm erg\ s^{-1}}\, E_{0,51}^{4/7} M_{10}^{-1/7} R_{0,500}^{4/7} v_{6000}^{3/7} T_{\rm i,6000}^{12/7}, \tag{32}$$

obtained by equating the plateau duration neglecting heating ($H = 0$; Equation (17)) with the timescale of Equation (29). For large heating rates $H > H_{\rm cr}$, the first regime in Equation (31) vanishes, because heating has already become important even prior to the recombination phase.

In either case, as long as the heating is present, the photosphere at late times $t > t_{\rm diff}^{\rm rec}$ or $t_{\rm pl,Popov}$ begins to shrink as $x \propto t^{-1}$ (following the final regime of Equation (31)) and never reaches $x = 0$, as in the no-heating case $H = 0$. Again defining the plateau duration as when the ejecta becomes optically thin (or enters the nebular phase), $x\tau = 1$, in the presence of a heating source we find

$$t_{\rm pl} \simeq \left(\frac{v}{c}\right)^{1/6}\left(\frac{H}{H_{\rm cr}}\right)^{1/6} t_{\rm thin} = \left(\frac{3^2\kappa^2 M^2 H}{2^6\pi^3\sigma_{\rm SB} T_{\rm i}^4 v^6}\right)^{1/6} \simeq 340\ {\rm day}\ M_{10}^{1/3} v_{6000}^{-1} T_{\rm i,6000}^{-2/3} H_{43}^{1/6}, \tag{33}$$

where

$$t_{\rm thin} = \left(\frac{3\kappa M}{4\pi v^2}\right)^{1/2} \simeq 780\ {\rm day}\ M_{10}^{1/2} v_{6000}^{-1} \tag{34}$$

is the time the ejecta becomes optically thin assuming full ionization. Equating Equation (33) with Equation (17) gives the heating rate above which the plateau duration is significantly boosted relative to the zero-heating case:

$$H_{\rm min} = \left(\frac{c}{v}\right)\left(\frac{t_{\rm pl,Popov}}{t_{\rm thin}}\right)^6 H_{\rm cr} \simeq 3.9 \times 10^{40}\ {\rm erg\ s^{-1}}\, E_{0,51}^{6/7} M_{10}^{-5/7} R_{0,500}^{6/7} v_{6000}^{15/7} T_{\rm i,6000}^{4/7}. \tag{35}$$

Note that while heating can extend the plateau duration in accordance with Equation (33), the duration is ultimately limited by when the ejecta becomes optically thin/nebular (Equation (34)). The latter limit is achieved for very powerful heating sources, which keep the ejecta fully ionized to late times. However, as we shall discuss, sufficiently powerful energy sources also act to accelerate the ejecta, hastening the nebular phase (Equation (34)).

3.2. With Acceleration

We now consider the effects of ejecta acceleration, which modifies the characteristic timescales ($t_{\rm diff}$ and $t_{\rm pl}$) that depend on v. Because the internal energy evolution is not modified from Equation (26) until the photon diffusion time, Equation (8) can be rewritten using the approximation $R \simeq vt$:

$$\frac{dv}{dt} = \frac{5E}{3MR} \simeq \begin{cases} \dfrac{5t_0 E_0}{3Mvt^2} & : t < t_{\rm h}, \\ \dfrac{5H}{3Mv} & : t_{\rm h} < t < t_{\rm diff}^{\rm acc}. \end{cases} \tag{36}$$

Here, $t_{\rm diff}^{\rm acc}$ is the diffusion timescale, now including the effects of acceleration, which in general will differ from Equation (4), as described below. Equation (36) can be integrated to obtain

$$v \simeq \begin{cases} \sqrt{v_0^2 + v_0^2\left(1 - \dfrac{t_0}{t}\right)} & : t < t_{\rm h}, \\ \sqrt{v_0^2 + v_0^2\left(1 - \dfrac{t_0}{t_{\rm h}}\right) + \dfrac{10H(t - t_{\rm h})}{3M}} & : t_{\rm h} < t < t_{\rm diff}^{\rm acc}, \end{cases} \tag{37}$$

where v_0 is the initial ejecta velocity. As discussed earlier, for $t < t_{\rm h}$, the velocity increases and asymptotes to $v = \sqrt{2}\, v_0$ at the expense of the initial internal energy, regardless of any heating source. For $t > t_{\rm h}$, the acceleration by PdV work becomes significant on the timescale

$$t_{\rm acc} = \frac{3Mv_0^2}{5H} \simeq 22\ {\rm day}\ M_{10} v_{0,4000}^2 H_{45}^{-1}, \tag{38}$$

as determined by the condition that the injected energy be comparable to the ejecta kinetic energy ($t_{\rm acc} H \simeq E_{\rm kin}$). Here, $v_0 = 4000 v_{0,4000}$ km s^{-1}. Therefore, the velocity evolution until $t < t_{\rm diff}^{\rm acc}$ can be summarized as

$$v \simeq \sqrt{2}\, v_0 \begin{cases} 1 & : t < t_{\rm acc}, \\ \left(\dfrac{t}{t_{\rm acc}}\right)^{1/2} & : t_{\rm acc} < t < t_{\rm diff}^{\rm acc}. \end{cases} \tag{39}$$

The diffusion timescale is obtained by substituting Equation (39) into Equation (4) and setting $t = t_{\rm diff}^{\rm acc}$:

$$t_{\rm diff}^{\rm acc} = \left(\frac{27\kappa^2 M^3}{160\pi^2 c^2 H}\right)^{1/5} \simeq 82\ {\rm day}\ M_{10}^{3/5} H_{45}^{-1/5}. \tag{40}$$

We find that after radiative cooling becomes important for $t > t_{\rm diff}^{\rm acc}$, the internal energy starts to decline again, following Equation (26). The equation of motion then takes the form $dv/dt \propto 1/(vt)^2$ and gives a similar solution to Equation (37) for $t < t_{\rm h}$. We can thus regard acceleration as effectively ceasing at $t_{\rm diff}^{\rm acc}$. The maximal velocity attained for $t_{\rm h} < t < t_{\rm diff}^{\rm acc}$ is given by Equations (39) and (40):

$$v_{\rm max} \simeq \left(\frac{25\kappa H^2}{3\pi c M}\right)^{1/5} \simeq 11,000\ {\rm km\ s^{-1}}\, M_{10}^{-1/5} H_{45}^{2/5}. \tag{41}$$

The corresponding effective temperature evolution is obtained by substituting Equations (39) or (41) into Equation (27):

$$T_{\rm eff} = \begin{cases} \left(\dfrac{c^2 H}{30\kappa^2\sigma_{\rm SB}^2 M t}\right)^{1/8} & : t_{\rm acc} < t < t_{\rm diff}^{\rm acc}, \\ \left(\dfrac{9c^2M^2H}{2^{10}5^4\pi^3\sigma_{\rm SB}^5\kappa^2 t^{10}}\right)^{1/20} & : t_{\rm diff}^{\rm acc} < t. \end{cases} \quad (42)$$

During the acceleration phase, the effective temperature remains almost constant and recombination starts after $t_{\rm diff}^{\rm acc}$, as in the constant-velocity case.[9] This timescale is obtained by equating Equation (42) with $T_{\rm i}$:

$$t_{\rm i}^{\rm acc} = \left(\frac{9c^2M^2H}{2^{10}5^4\pi^3\sigma_{\rm SB}^5\kappa^2 T_{\rm i}^{20}}\right)^{1/10} \simeq 350\ {\rm day}\ M_{10}^{1/5} T_{\rm i,6000}^{-1/2} H_{45}^{1/10}. \quad (43)$$

Once recombination begins at $t_{\rm i}^{\rm acc}$, the following evolution is identical to the constant-velocity case. In particular, the plateau duration is obtained by substituting the maximal velocity, Equation (41), into Equation (33):

$$t_{\rm pl}^{\rm acc} = \left(\frac{3^{16}\kappa^4 c^6 M^{16}}{2^{30}5^{12}\pi^9\sigma_{\rm SB}^5 T_{\rm i}^{20} H^7}\right)^{1/30} \simeq 400\ {\rm day}\ M_{10}^{8/15} T_{\rm i,6000}^{-2/3} H_{45}^{-7/30}. \quad (44)$$

Contrary to the constant-velocity case, the plateau duration now shrinks with increasing H as a result of the higher ejecta expansion speed.

The maximal plateau duration is thus obtained by the maximal heating rate, which does not appreciably affect the ejecta dynamics. Since the acceleration of the ejecta ceases on the diffusion time, we can obtain this critical heating rate by equating $t_{\rm acc}$ with $t_{\rm diff}^{\rm acc}$ (Equation (40)):

$$H_{\rm pl,max} = \left(\frac{3\pi c M v^5}{25\kappa}\right)^{1/2} \simeq 2.3\times10^{44}\ {\rm erg\ s^{-1}}\ M_{10}^{1/2} v_{6000}^{5/2}, \quad (45)$$

which when substituted into Equation (33) gives the corresponding maximal plateau duration:

$$t_{\rm pl,max} = \left(\frac{3^5\kappa^3 c M^5}{2^{12}5^2\pi^5\sigma_{\rm SB}^2 T_{\rm i}^8 v^7}\right)^{1/12} \simeq 570\ {\rm day}\ M_{10}^{5/12} v_{6000}^{-7/12} T_{\rm i,6000}^{-2/3}. \quad (46)$$

Above, we have assumed that the acceleration terminates on the diffusion time assuming fully ionized ejecta; however, this transition can occur earlier if the ejecta recombines first. Because recombination occurs when $T_{\rm eff} = T_{\rm ion}$, the maximal heating rate in this case is $H_{\rm cr}$ (Equation (12)). When the condition

$$E_{\rm kin} < H_{\rm cr} t_{\rm diff} \quad (47)$$

is satisfied, the critical heating rate obeys $H_{\rm cr} > H_{\rm pl,max}$, resulting in a maximal plateau duration:

$$t_{\rm pl,max} = \left(\frac{3^3\kappa^3 M^3}{2^6\pi^3 c v^5}\right)^{1/6} \simeq 410\ {\rm day}\ M_{10}^{1/2} v_{6000}^{-5/6}. \quad (48)$$

For very large heating rates, the ejecta bypasses the recombination phase entirely and proceeds to become optically thin while still fully ionized. By equating Equation (44) with Equation (43), we obtain the critical heating rate above which the recombination phase vanishes:

$$H_{\rm thin} = \left(\frac{c}{v}\right) H_{\rm cr} = 3\kappa\sigma_{\rm SB} T_{\rm i}^4 M \simeq 1.5\times10^{45}\ {\rm erg\ s^{-1}}\ M_{10} T_{\rm i,6000}^4. \quad (49)$$

The nebular phase in this case begins at

$$t_{\rm thin}^{\rm acc} = \left(\frac{3^7\kappa^3 c^2 M^7}{2^{10}5^4\pi^3 H^4}\right)^{1/10} \simeq 430\ {\rm day}\ M_{10}^{7/10} H_{45}^{-2/5}, \quad (50)$$

obtained by substituting Equation (41) into Equation (34).

Figure 2 illustrates the key timescales as a function of the heating rate. The black dotted and solid curves show the recombination time $t_{\rm i}$ and plateau duration $t_{\rm pl}$, respectively, as obtained by solving the equations directly, as in Figure 1. Their behavior agrees with our analytical formulae, supporting the above arguments. A dotted curve denotes the recombination time $t_{\rm i}$ at which the effective temperature equals the recombination temperature. For small heating rates $H < H_{\rm cr} \simeq 3\times10^{43}\ {\rm erg\ s^{-1}}$ (Equation (12)), this timescale is independent of H and identical to the Popov formula (Equations (15) and (28)). For heating rates approaching the critical value, $H \simeq H_{\rm cr}$, the recombination time increases rapidly (representing the gap in $t_{\rm i}$ in Equation (28)), because heating begins to affect the thermal evolution for $t \gtrsim t_{\rm h}$ (Equation (24)), which significantly delays the recombination. Once heating starts to affect the

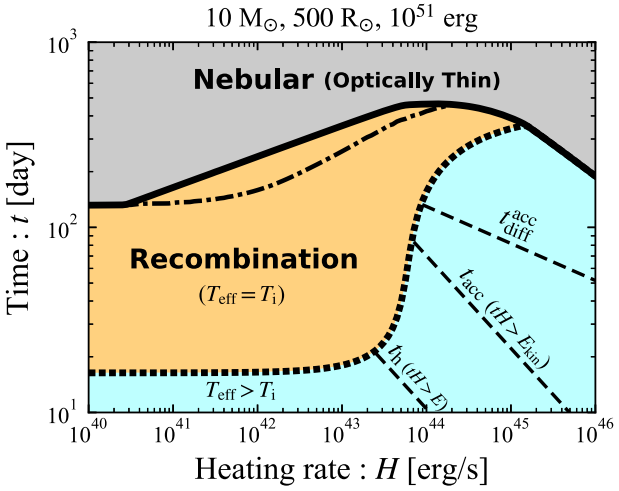

Figure 2. Key timescales as a function of the assumed constant ejecta heating rate. The dotted and solid curves denote the recombination time $t_{\rm i}$ and plateau duration $t_{\rm pl}$, respectively. The light blue, orange, and gray shaded regions represent the photospheric phase with $T_{\rm eff} > T_{\rm i}$, the recombination phase ($T_{\rm eff} = T_{\rm i}$), and the nebular phase (optically thin), respectively. The dashed–dotted curve shows $t_{\rm diff}^{\rm rec}$, after which the luminosity begins to track the input heating rate. The dashed lines represent three characteristic timescales, on which the heating appreciably alters the thermal ($t_{\rm h}$, Equation (24)) and dynamical ($t_{\rm acc}$, Equation (38)) evolution of the ejecta, as well as the diffusion time for maximally accelerated ejecta ($t_{\rm diff}^{\rm acc}$, Equation (40)).

[9] Recombination occurs during the acceleration phase ($t_{\rm acc} < t < t_{\rm diff}^{\rm acc}$) for $H \lesssim \left(\dfrac{3^4 5^2 \sigma_{\rm SB}^5 \kappa^6 M^4 T_{\rm i}^{20}}{\pi c^6}\right)^{1/3} \simeq 7.8\times10^{42}\ {\rm erg\ s^{-1}}\ M_{10}^{4/3} T_{\rm i,6000}^{20/3}$. Such small heating rates do not significantly impact the ejecta's dynamics.

dynamics of the ejecta as well for $t_{\rm acc} < t < t_{\rm diff}^{\rm acc}$ (Equations (38) and (40)), the recombination time increases more gradually, as $t_{\rm i}^{\rm acc} \propto H^{1/10}$ (Equation (43)).

The solid curve in Figure 2 depicts the plateau time $t_{\rm pl}$ at which the ejecta becomes optically thin and enters the nebular phase. For heating rates $H \gtrsim H_{\rm min} \simeq 4 \times 10^{40}\,{\rm erg\,s^{-1}}$ (Equation (35)), the plateau duration is prolonged from the Popov formula (Equation (17)) as $t_{\rm pl} \propto H^{1/6}$ (Equation (28)), where $H_{\rm min}$ is smaller than the critical rate $H_{\rm cr}$, because the heating plays a role only during the recombination phase. When the acceleration becomes significant for higher heating rates, the plateau duration shrinks as $t_{\rm pl}^{\rm acc} \propto H^{-7/30}$ (Equation (44)) upon further heating, due to the higher ejecta velocity. The maximal allowed plateau duration for a given ejecta mass (Equation (46)) is thus obtained for the maximal heating rate (Equation (45)) that does not appreciably accelerate the ejecta. For the highest heating rates $H > H_{\rm thin} \simeq 2 \times 10^{45}\,{\rm erg\,s^{-1}}$ (Equation (49)), the ejecta remains ionized throughout its entire evolution and the recombination phase disappears. The nebular phase also begins earlier for the largest hearing rate as $t_{\rm thin}^{\rm acc} \propto H^{-2/5}$ (Equation (50)), because of the higher velocity.

As discussed around Equation (40), the plateau duration can observationally be identified as when the luminosity drops rapidly and begins to track the ejecta heating rate (e.g., S. Valenti et al. 2016). In our framework, this transition happens at $t_{\rm diff}^{\rm rec}$, as indicated by the dashed–dotted curve in Figure 2. By definition, this transition occurs before $t_{\rm pl}$ and thus provides a conservative lower limit on the plateau duration, while it does not change our quantitative results significantly.

Figure 3 shows the "trajectory" of plateau duration and luminosity, achieved for different heating rates, in the duration–luminosity phase-space diagram of optical transients (M. M. Kasliwal 2011). As with the Popov formulae (Equation (18)), we define the plateau luminosity by dividing the total radiated energy up to the nebular phase by the plateau duration (when the ejecta becomes optically thin):

$$L_{\rm pl} \equiv \frac{E_{\rm rad}}{t_{\rm pl}} \quad \text{and} \quad E_{\rm rad} = \int_0^{t_{\rm pl}} L dt. \tag{51}$$

For $H \lesssim H_{\rm thin}$, the total radiated energy is dominated by the recombination phase. Initially, as the heating rate increases, only the plateau duration increases (Figure 1, Equation (33)). This incremental change is reflected as only a modest flattening of the light curve after the main plateau for $t_{\rm diff}^{\rm rec} < t < t_{\rm pl}$, which does not contribute to the radiated energy, causing the plateau luminosity to remain unchanged or to slightly decrease. As H increases further, both the luminosity and duration increase up to the critical heating rate that gives the maximal plateau duration. In this regime, the radiated energy is dominated by the recombination phase:

$$E_{\rm rad} \simeq \int_{t_{\rm i}}^{t_{\rm pl}} L dt = 4\pi v^2 \sigma_{\rm SB} T_{\rm i}^4 \int_{t_{\rm i}}^{t_{\rm pl}} (xt)^2 dt \simeq H t_{\rm pl}, \tag{52}$$

where the last equality makes use of $x \simeq (H/H_{\rm cr})^{1/2} t_{\rm diff}/t$ (Equation (31)) and assumes $t_{\rm pl} \gg t_{\rm i}$. Perhaps surprisingly, this expression also provides a reasonable estimate of the the plateau luminosity even for larger heating rates, because the SN luminosity closely tracks H after the diffusion timescale (see Figure 1). By solving Equations (33), (44), and (50) for H, we obtain the following scaling relations:

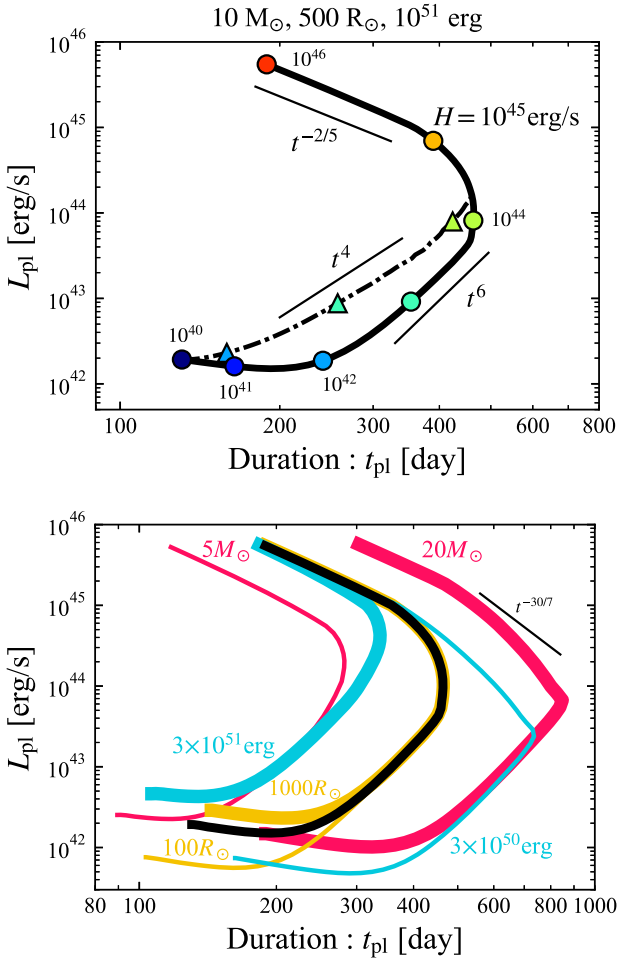

Figure 3. Top: trajectory of plateau duration and luminosity for different constant heating rates (increasing in order-of-magnitude increments from blue to red) for a canonical explosion of ejecta mass $10M_\odot$, energy 10^{51} erg, and $500R_\odot$ progenitor radius. The circles and triangles along the curve show the results corresponding to the calculations in Figure 1 with the same color scheme. Bottom: the same as the top panel, but for different ejecta properties (total mass, initial energy, and progenitor radius), as marked.

$$L_{\rm pl} \simeq \begin{cases} 3.9 \times 10^{42}\,{\rm erg\,s^{-1}}\, E_{\rm kin,0,51}^3 M_{10}^{-5} T_{\rm i,6000}^4 \left(\dfrac{t_{\rm pl}}{300\,{\rm day}}\right)^6 \\ \qquad\qquad : H < H_{\rm pl,max}, \\ 3.5 \times 10^{45}\,{\rm erg\,s^{-1}}\, M_{10}^{16/7} T_{\rm i,6000}^{-20/7} \left(\dfrac{t_{\rm pl}}{300\,{\rm day}}\right)^{-30/7} \\ \qquad\qquad : H_{\rm pl,max} < H < H_{\rm thin}, \\ 2.5 \times 10^{45}\,{\rm erg\,s^{-1}}\, M_{10}^{7/4} \left(\dfrac{t_{\rm pl}}{300\,{\rm day}}\right)^{-5/2} \\ \qquad\qquad : H_{\rm thin} < H, \end{cases} \tag{53}$$

where we have again replaced $t_{\rm pl}^{\rm acc}$ in the middle and $t_{\rm thin}^{\rm acc}$ in the bottom regimes with $t_{\rm pl}$, retaining the same notation. We have also substituted v from Equation (7).

The top panel of Figure 3 depicts the $L_{\rm pl} - t_{\rm pl}$ trajectories of our light-curve models from Figure 1, illustrating how our analytic scaling relations (Equation (53)) can reasonably

reproduce the results of our full numerical calculations. For the specific ejecta properties chosen, the middle regime of Equation (53) does not clearly appear, because the two characteristic heating rates, $H_{\rm pl,max} \sim H_{\rm thin}$, are not well separated (though this regime appears more clearly for other parameter choices; see below). The dashed–dotted curve shows how the trajectory changes if one were instead to take $t_{\rm diff}^{\rm rec}$ (the time at which the light curve starts to track the central heating source) as the definition of plateau duration. This alternative definition predicts a slightly different scaling relationship:

$$L_{\rm pl} \simeq 2.3 \times 10^{43}\,{\rm erg\ s^{-1}}\, E_{\rm kin,0,51}^{3/2} M_{10}^{-5/2} T_{\rm i,6000}^{4} \left(\frac{t_{\rm pl}}{300\,{\rm day}}\right)^{4}.$$

The bottom panel of Figure 3 shows similar $L_{\rm pl} - t_{\rm pl}$ trajectories, but for different ejecta and explosion properties. While the shape of the trajectory does not change significantly (except for the middle regime in Equation (53) appearing in some cases), it shifts from side to side, depending on the kinetic energy and ejecta mass. These general behaviors can be simply understood by the longer diffusion timescale/plateau duration that arises for more massive and/or less-energetic/slower ejecta. Consistent with Equation (53), the trajectory depends only weakly on the initial progenitor radius R_0, except in the weakly heated regime $H < H_{\rm min}$ corresponding to the standard Popov limit.

4. Physically Motivated Heating Sources

We now apply our model to several physically motivated ejecta heating sources: radioactive ^{56}Ni/^{56}Co decay; rotational or accretion power from a central compact object (neutron star or black hole); and shock interaction with circumstellar gas. Some of these heating sources may be spatially localized within the ejecta, rendering our one-zone assumption questionable. However, we believe our model still provides useful physical insight and a reasonable approximation for the impact on the plateau duration in these cases, particularly in light of the uncertainties that impact the exact form of the heating in many of these cases. Indeed, our results for magnetar-powered light curves match well the results obtained by radiation hydrodynamic simulations, which make the extreme assumption of a completely centralized heating source (see Section 4.2). We also give a more detailed justification of the one-zone model in Appendix A.

The evolution of the heating rate can in most of these cases be approximately described as a constant heating rate up to some break time $t_{\rm br}$, followed by a power-law decay, viz.

$$H(t) = \begin{cases} \widetilde{H} & :t < t_{\rm br}, \\ \widetilde{H}\left(\dfrac{t}{t_{\rm br}}\right)^{-\alpha} & :t_{\rm br} < t. \end{cases} \tag{54}$$

The normalization $\widetilde{H}$, break time $t_{\rm br}$ and power-law exponent $\alpha > 0$ depend on the energy source in question (see Figure 4). In Appendix B, we rederive several of the analytic expressions from the constant-heating case (Section 3) for this more complex heating evolution.

4.1. Radioactive Decay Heating

It is well known that heating from radioactive decay extends the plateau duration in SNeIIP (e.g., T. R. Young 2004; D. Kasen & S. E. Woosley 2009; M. C. Bersten et al. 2011; E. Nakar et al. 2016; J. A. Goldberg et al. 2019; A. Kozyreva et al. 2019). In particular, the heating rate of the ^{56}Ni→^{56}Co→^{56}Fe decay chain can be written (D. K. Nadyozhin 1994) as

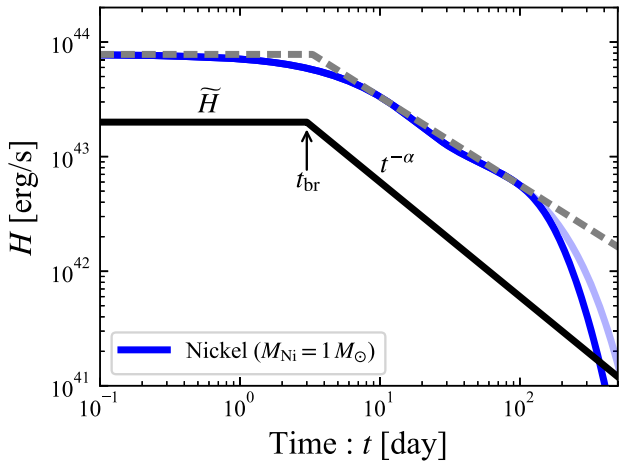

Figure 4. The physically motivated ejecta heating sources presented in this paper can in most cases be approximated as a constant heating rate $\widetilde{H}$, followed after a break at time $t_{\rm br}$ by a power-law decay $\propto t^{-\alpha}$ of the form of Equation (54), shown here schematically with a black solid line. The gray dashed line denotes such a form's fit to the ^{56}Ni→^{56}Co→^{56}Fe decay chain, the latter shown as the dark (light) solid blue line in the case with (without) the gamma-ray energy deposition factor $f_{\rm dep}$.

$$H(t) = M_{\rm Ni}[(\varepsilon_{\rm Ni} - \varepsilon_{\rm Co})e^{-t/t_{\rm Ni}} + \varepsilon_{\rm Co} e^{-t/t_{\rm Co}}], \tag{55}$$

where $M_{\rm Ni}$ is the nickel mass, $\varepsilon_{\rm Ni} = 3.9 \times 10^{10}\,{\rm erg\,g^{-1}\,s^{-1}}$, $\varepsilon_{\rm Co} = 6.8 \times 10^{9}\,{\rm erg\,g^{-1}\,s^{-1}}$, $t_{\rm Ni} = 8.8$ days, and $t_{\rm Co} = 111.3$ days. The total energy released by radioactive decay,

$$E_{\rm Ni} \equiv \int_0^\infty H(t)dt \simeq M_{\rm Ni}[t_{\rm Ni}(\varepsilon_{\rm Ni} - \varepsilon_{\rm Co}) + t_{\rm Co}\varepsilon_{\rm Co}],$$
$$\simeq 1.8 \times 10^{48}\,{\rm erg}\left(\frac{M_{\rm Ni}}{10^{-2}\,M_\odot}\right), \tag{56}$$

is typically much smaller than the ejecta kinetic energy for values $M_{\rm Ni} \sim 10^{-3}$–$0.1 M_\odot$ characteristic of SNeIIP (e.g., M. Hamuy 2003; J. P. Anderson et al. 2014; S. Valenti et al. 2016; T. Müller et al. 2017; J. P. Anderson 2019; L. Martinez et al. 2022b). Because ejecta acceleration by radioactive decay energy is generally negligible, it is safe to assume a constant ejecta speed in analytic estimates.

Most of the energy released by the ^{56}Ni decay chain is carried by gamma rays, which at sufficiently late times leak out of the ejecta without depositing energy. This suppression effect on the heating rate (Equation (55)) can be included by a multiplying deposition factor (D. J. Jeffery 1999):

$$f_{\rm dep}(t) = 1 - e^{-x\tau_\gamma}, \tag{57}$$

where $\tau_\gamma = \kappa_\gamma \rho R$ is the gamma-ray optical depth and $\kappa_\gamma = 0.03\,{\rm cm^2\,g^{-1}}$ is the associated opacity (D. A. Swartz et al. 1995). After the ejecta becomes optically thin to gamma rays at $\simeq (\kappa_\gamma/\kappa)^{1/2} t_{\rm thin} \simeq 230$ days, the deposition efficiency steeply declines, $f_{\rm dep}(t) \propto t^{-2}$.

Figure 5 depicts the time evolution of the same quantities (luminosity, photosphere radius, and photosphere velocity) shown in Figure 1 for the time-dependent $H(t)$ and $f_{\rm dep}(t)$

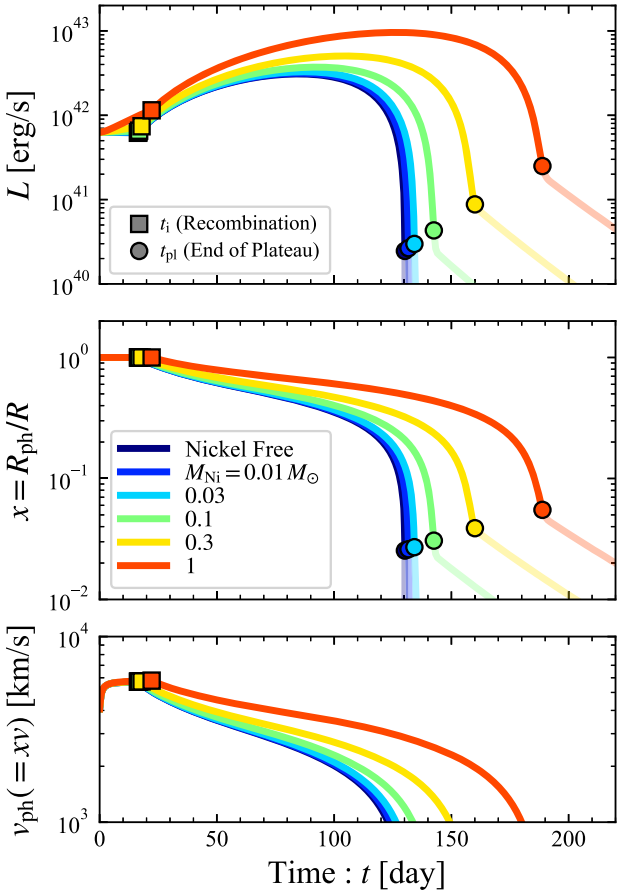

Figure 5. Time evolution of the bolometric luminosity, location, and velocity of the photosphere (similar to Figure 1) for models incorporating the exact ^{56}Ni decay-chain heating, for different values of the ^{56}Ni mass, as marked.

described by Equations (55) and (57). As expected, the recombination phase grows longer for larger ^{56}Ni masses. However, different from the case of constant heating, the ejecta becomes optically thin prior to when the luminosity begins to track the input heating rate (i.e., the timescale $t_{\rm diff}^{\rm rec}$ is not reached), because of the sharp drop-off in the heating rate at $t \gtrsim 100$ days (Figure 4).

Figure 6 shows the key timescales from Figure 2 but now as a function of ^{56}Ni mass instead of the generic heating rate. Although we consider nickel masses that range up to the total ejecta mass ($M = 10\,M_\odot$), such extreme yields of radioactive material are obviously unphysical, except perhaps in some PISNe. For nickel masses typical of SNeIIP, the onset time of the recombination phase t_i is essentially unaffected by radioactive heating. Though still relatively modest, lengthening of the plateau duration with increasing ^{56}Ni mass is more readily apparent.

The above results obtained by employing the exact heating rate (Equation (55)) can also be understood quantitatively within our analytical framework, following Appendix B. Figure 4 shows that the heating rate of the ^{56}Ni decay chain at $t \lesssim 100$ days is well approximated as a broken-power-law function of the form of Equation (54), with

$$\widetilde{H} = M_{\rm Ni}\varepsilon_{\rm Ni} \simeq 7.8 \times 10^{41}\,{\rm erg\ s^{-1}} \left(\frac{M_{\rm Ni}}{10^{-2}\,M_\odot}\right),$$

$$t_{\rm br} = 3.3\ {\rm days},$$

$$\alpha = 0.77.$$

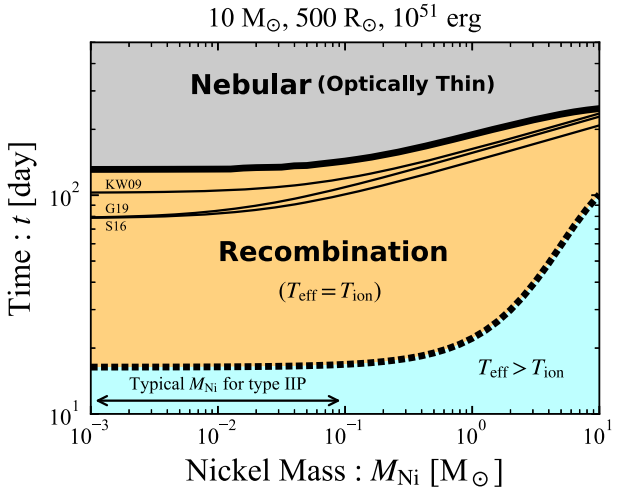

Figure 6. The same as Figure 2 but for ^{56}Ni decay-chain heating. The thin solid lines show analytic estimates for the plateau duration from the literature (D. Kasen & S. E. Woosley 2009; T. Sukhbold et al. 2016; J. A. Goldberg et al. 2019, from top to bottom). A double-headed arrow denotes the typical range of ^{56}Ni masses inferred for SNeIIP, $M_{\rm Ni} \simeq 10^{-3}$–$0.1\,M_\odot$.

Neglecting the gamma-ray deposition factor, our analytic estimate for the plateau duration for these parameters follows from Equation (B8):

$$t_{\rm pl} \simeq 200\ {\rm day} \left(\frac{M_{\rm Ni}}{0.1\,M_\odot}\right)^{0.15} E_{0,51}^{-0.44} M_{10}^{0.74}, \quad (58)$$

where we have omitted the dependence on T_i and eliminated the v-dependence using Equation (7), by equating the initial internal and kinetic energies $E_0 = E_{\rm kin,0}$. By equating Equation (58) with Equation (17), we obtain the minimal nickel mass to modify the plateau duration:

$$M_{\rm Ni,min} \simeq 8.1 \times 10^{-3}\,M_\odot\, R_{0,500}^{0.97} E_{0,51}^{1.8} M_{10}^{-1.4}. \quad (59)$$

We now compare these results with previous works. D. Kasen & S. E. Woosley (2009) present a heuristic argument for how to include ^{56}Ni heating as a correction to the analytic plateau duration of D. V. Popov (1993), described by

$$t_{\rm pl} = t_{\rm pl,Popov} \times \left[1 + C_{\rm f}\left(\frac{M_{\rm Ni}}{M_\odot}\right) E_{\rm SN,51}^{-1/2} M_{10}^{-1/2} R_{0,500}^{-1}\right]^{1/6}, \quad (60)$$

where $E_{\rm SN}(=E_0 + E_{\rm kin,0})$ is the total explosion energy. The constant $C_{\rm f}$ is sensitive to the ejecta density profile and distribution of ^{56}Ni in the ejecta and can be calibrated by radiation transport simulations, with D. Kasen & S. E. Woosley (2009) finding $C_{\rm f} \simeq 21$, T. Sukhbold et al. (2016) finding $\simeq$50, and J. A. Goldberg et al. (2019) finding $\simeq$87. Equation (60) is shown as the thin solid curves in Figure 6 for different values of $C_{\rm f}$. Here, the nickel-free plateau duration $t_{\rm pl,Popov}$ is not given by Equation (17) but rather is taken directly from each reference (see the footnote at the end of Section 2). Our result (thick solid curve) is broadly consistent with these numerically calibrated analytic expressions.

While our results and previous studies show reasonable agreement, there are differences between them. From Equation (60), the minimum nickel mass required to impact

the plateau duration can be estimated by equating the second term in the square bracket with unity:

$$M_{\rm Ni,min} \simeq 4.8 \times 10^{-2}\, M_\odot \left(\frac{C_{\rm f}}{21}\right)^{-1} E_{\rm SN,51}^{1/2} M_{10}^{1/2} R_{500}. \quad (61)$$

For nickel masses larger than this value (which corresponds to a $2^{1/6} \simeq 12\%$ increase in $t_{\rm pl}$ versus the Ni-free case), the plateau duration is considerably increased, now scaling with the ejecta properties according to

$$t_{\rm pl} \propto M_{\rm Ni}^{1/6} E_{\rm SN}^{-1/4} M^{5/12} \simeq M_{\rm Ni}^{0.17} E_{\rm SN}^{-0.25} M^{0.42}, \quad (62)$$

where we use Equation (21) for $t_{\rm pl,Popov}$. The exponents on the ejecta mass and explosion energy here differ from our analytical expressions in Equations (58) and (59), in particular with the dependence of $M_{\rm Ni,min}$ on M changing sign. This disagreement results from the different ways that ^{56}Ni heating is treated in our formula versus that of D. Kasen & S. E. Woosley (2009). We define $t_{\rm pl}$ by $x\tau = 1$ and account for ^{56}Ni heating during the plateau phase, which delays the recession of the recombination front $x(t)$. By contrast, D. Kasen & S. E. Woosley (2009) consider the heat from radioactive decay to boost the internal energy such that heating effectively occurs immediately at $t_{\rm Ni}$ and $t_{\rm Co}$ (see their Equation (9)). Therefore, in our formulation, increasing M slows the intrinsic evolution of x, thus allowing a lower $M_{\rm Ni}$ to significantly increase $t_{\rm pl} > t_{\rm pl,Popov}$. In the D. Kasen & S. E. Woosley (2009) scenario, increasing M boosts the internal energy available at a given t ($>t_{\rm Ni}$ or $t_{\rm Co}$), due to the smaller adiabatic losses experienced for lower expansion velocity (at fixed $E_{\rm SN}$), which thus requires higher $M_{\rm Ni}$ to generate enough heating to boost $t_{\rm pl} > t_{\rm pl,Popov}$. We remark that the exponent of M in our $M_{\rm Ni,min}$ depends on α as $M_{\rm Ni,min} \propto M^{\frac{5(3\alpha-10)}{28}}$.

4.2. Magnetar

Another frequently invoked central energy source is the spindown energy of a newly formed, rapidly spinning magnetized neutron star ("magnetar"; e.g., K. Maeda et al. 2007; D. Kasen & L. Bildsten 2010; S. E. Woosley 2010; E. Chatzopoulos et al. 2012; B. D. Metzger et al. 2015; T. Sukhbold & T. A. Thompson 2017). Assuming the Poynting luminosity of the magnetar wind, and the high-energy radiation it generates, to be thermalized within the ejecta (likely a good approximation at least at early times; I. Vurm & B. D. Metzger 2021), the heating-rate evolution will follow the standard magnetic dipole spindown rate (e.g., A. Spitkovsky 2006). The latter can be expressed in the form

$$H(t) = \frac{E_{\rm rot}}{t_{\rm sd}} \left(1 + \frac{t}{t_{\rm sd}}\right)^{-2}, \quad (63)$$

where $E_{\rm rot}$ and $t_{\rm sd}$ are the magnetar's initial rotational energy and spindown timescale, respectively. These quantities are roughly related to the initial spin period $P_{\rm i}$ and surface magnetic field strength B by

$$P_{\rm i} \simeq \left(\frac{2\pi^2 I}{E_{\rm rot}}\right)^{1/2} \simeq 1.4\ {\rm ms}\ E_{\rm rot,52}^{-1/2}, \quad (64)$$

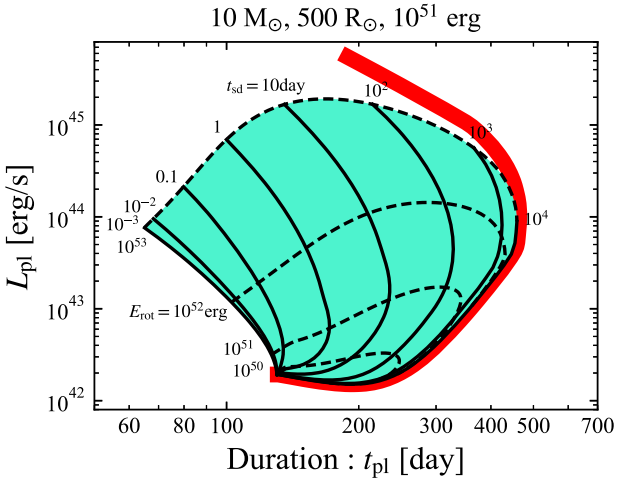

Figure 7. The same as Figure 3 but for heating by magnetar spindown. The black solid (dashed) curves show the contours for a fixed spindown timescale, $t_{\rm sd}$ (fixed magnetar rotation energy, $E_{\rm rot}$). The red thick curve shows the constant-heating case (see Figure 3), which bounds the high-$t_{\rm pl}$ edge of the parameter space.

$$B \simeq \left(\frac{c^3 I^2}{4R_{\rm NS}^6 E_{\rm rot} t_{\rm sd}}\right)^{1/2} \simeq 8.8 \times 10^{13}\ {\rm G}\ E_{\rm rot,52}^{-1/2} \left(\frac{t_{\rm sd}}{\rm day}\right)^{-1/2}, \quad (65)$$

where I and $R_{\rm NS}$ are the magnetar's moment of inertia and radius, respectively, and we adopt $I = 10^{45}\,{\rm g\,cm^2}$ and $R_{\rm NS} = 10\,{\rm km}$. However, we neglect this correspondence for simplicity, instead referring directly to $t_{\rm sd}$ and $E_{\rm rot}$. One hard constraint is that a magnetar cannot spin faster than its centrifugal breakup rate, which limits $E_{\rm rot} \lesssim 10^{53}\,{\rm erg}$ (B. D. Metzger et al. 2015). Additionally, different from heating due to radioactive decay or CSM interaction, energy input from the magnetar can appreciably accelerate the SN ejecta (e.g., D. Kasen et al. 2016; A. Suzuki & K. Maeda 2021).

Figure 7 shows the plateau duration and luminosity for a range of values $E_{\rm rot} = 10^{48}$–$10^{53}\,{\rm erg}$ and $t_{\rm sd} = 10^{-3}$–$10^{4}\,{\rm days}$, corresponding to physically allowed birth spin periods and magnetic field strengths. At a fixed spindown time, the plateau luminosity increases monotonically with $E_{\rm rot}$, while the plateau duration initially grows but then turns over and decreases for $E_{\rm rot} \gtrsim E_{\rm kin,0} = 10^{51}\,{\rm erg}$, once acceleration of the ejecta becomes significant.

The contours of fixed $t_{\rm sd}$ accumulate in the two extreme limits $t_{\rm sd} \to 0$ and ∞. For spindown times much shorter than the initial dynamical time $t_{\rm sd} \lesssim t_0 \sim 1\,{\rm day}$, the heating of the ejecta is effectively instantaneous. This leads to the acceleration of the ejecta at the expense of the deposited energy for $t \gtrsim t_0$, with the subsequent evolution practically described by replacing $E_0 \to E_{\rm rot}$ and $v \to \sqrt{10E_{\rm rot}/3M}$ in the Popov formula. Because for early energy injection, the ejecta loses memory of when energy is deposited, the contours become independent of $t_{\rm sd}$ for small $t_{\rm sd} \lesssim 10^{-2}\,{\rm days}$.

In the opposite limit $t_{\rm sd} \to \infty$, the contours asymptote to the constant-heating case. For heating times longer than the plateau duration $t_{\rm sd} \gtrsim t_{\rm pl,Popov} \sim 10^2\,{\rm days}$, the magnetar provides what is effectively a constant heating source during the plateau. The red curve shows the constant-heating-rate limit (see Figure 3),

which bounds the allowed plateau duration in the magnetar model.

Most previous applications of magnetar engines are to hydrogen-poor SLSNeII; however, a few works have explored the impact of a magnetar on hydrogen-rich SN light curves using numerical calculations (T. Sukhbold & T. A. Thompson 2017; L. Dessart & E. Audit 2018; M. Orellana et al. 2018). While these works adopt different definitions for the plateau duration and luminosity, precluding a quantitative comparison, their findings are broadly compatible with the simpler analytic estimates presented here.

4.3. Accreting Compact Object

Another potential heating source of the SN ejecta is a relativistic jet[10] or accretion disk outflow, powered by mass accretion on the central black hole or neutron star (e.g., J. Dexter & D. Kasen 2013; T. J. Moriya et al. 2018; N. Kaplan & N. Soker 2020). The rate of fallback accretion is expected to decline at late times as $\dot{M}_{\rm fb} \propto t^{-5/3}$ (F. C. Michel 1988; R. A. Chevalier 1989), following an initial phase defined by the radial structure of the progenitor star (J. Dexter & D. Kasen 2013; R. Perna et al. 2014; T. J. Moriya et al. 2019), particularly its radius (e.g., R. Perna et al. 2018). The manner in which the mass fallback is processed by the central accretion disk or its outflows can also modify the accretion rate reaching the central compact object and hence the heating rate (e.g., B. D. Metzger et al. 2008). We encapsulate these uncertainties by adopting a broken-power-law heating rate, similar to the magnetar case:

$$H(t) = \frac{(\alpha_{\rm fb}-1)E_{\rm acc}}{t_{\rm fb}}\left(1+\frac{t}{t_{\rm fb}}\right)^{-\alpha_{\rm fb}}, \quad (66)$$

where the total available energy $E_{\rm acc}$ now scales with the accreted mass $M_{\rm acc}$ for some assumed efficiency $\eta = E_{\rm acc}/M_{\rm acc}c^2$, and $t_{\rm fb}$ is the characteristic fallback time. The latter is generally expected to scale with the fallback time of the stellar envelope:

$$t_{\rm fb} \sim \frac{1}{\sqrt{G\rho_\star}} \simeq 130\ {\rm day}\left(\frac{M_\star}{10\,M_\odot}\right)^{-1/2}\left(\frac{R_\star}{500\,R_\odot}\right)^{3/2}, \quad (67)$$

where $\rho_\star \equiv 3M_\star/4\pi R_\star^3$ is the mean density of the star of mass $M_\star$ and radius $R_\star$. We consider the post-break exponent $\alpha_{\rm fb}$ as a free parameter. The $\alpha_{\rm fb}-1$ prefactor in Equation (66) follows from the normalization $E_{\rm acc} = \int_0^\infty H(t)dt$.

Figure 8 depicts the plateau duration and luminosity for different $\alpha_{\rm fb}$, $E_{\rm acc}$, and $t_{\rm fb}$, similar to the format of Figure 7. The colors of each shaded region correspond to the range of $t_{\rm pl}$ and $L_{\rm pl}$ for different ranges of $\alpha_{\rm fb} = 4/3$ to 4, as marked. The contours follow a similar shape to that of the magnetar heating (corresponding to $\alpha_{\rm fb} = 2$). The black solid and dashed curves represent the contours for fixed $E_{\rm acc}$ and $t_{\rm fb}$ for the special case $\alpha_{\rm fb} = 5/3$ (corresponding to a canonical fallback rate). For smaller exponents, the heating rate declines more slowly, increasing the plateau luminosity. As in the case of magnetar heating, the plateau duration is maximized for longer fallback

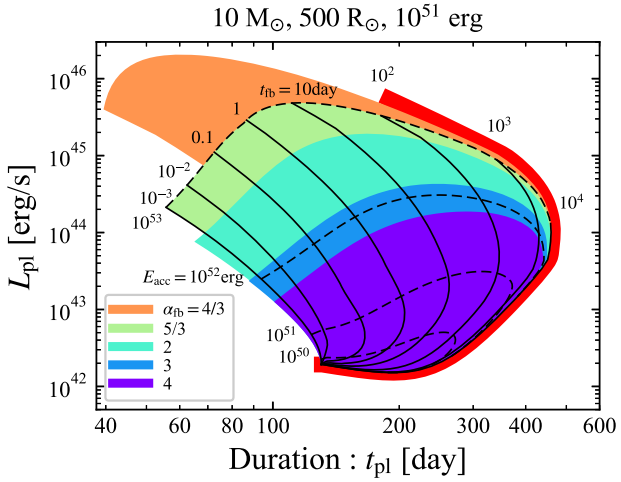

Figure 8. The same as Figure 3 but for heating by accretion onto a central compact object, following Equation (66). Each shaded region corresponds to the parameter space of plateau duration and luminosity for different values of the post-break index $\alpha_{\rm fb}$. The shaded regions are overlaid such that the curves for larger $\alpha_{\rm fb}$ cover part of the smaller-$\alpha_{\rm fb}$ curves. All values of $\alpha_{\rm fb}$ are bounded at the bottom by the constant-heating case. The region for $\alpha_{\rm fb} = 2$ essentially follows the magnetar heating case (see Figure 7). The black solid and dashed contours denote the cases of a fixed fallback timescale and total accretion energy for $\alpha_{\rm fb} = 5/3$. The red thick curve shows the case of a constant heating rate (see Figure 3), which bounds the high-$t_{\rm pl}$ edge of the parameter space (see also Figure 3).

timescales, but the attainable region is bounded by the limit of a constant heating rate.

4.4. CSM Shock Interaction

As a final heating source, we consider shock interaction between the SN ejecta and a CSM. While most of the modeling literature focuses on a CSM that is distributed spherically symmetrically around the explosion site (e.g., D. K. Khatami & D. N. Kasen 2024), this geometry confines the effects of shock heating to the outermost layers of the ejecta. While shock heating can in that case contribute to the early-time SN light curve by impacting the initial thermal energy imparted to these outer layers, it does not provide a sustained heating source embedded behind the photosphere that would affect the duration of the plateau and later-time SN evolution. We are thus motivated to consider the case of an aspherical CSM, confined into a disk or otherwise equatorially focused configuration surrounding the progenitor (J. M. Blondin et al. 1996; A. J. Van Marle et al. 2010; A. Vlasis et al. 2016; A. T. McDowell et al. 2018; P. Kurfürst & J. Krtička 2019; A. Suzuki et al. 2019; P. Kurfürst et al. 2020; T. Nagao et al. 2020), a geometry that is supported by some observations of Type IIn or otherwise peculiar SNe (N. N. Chugai & I. J. Danziger 1994; D. C. Leonard et al. 2000; J. E. Andrews et al. 2017, 2019; J. E. Andrews & N. Smith 2018; C. Bilinski et al. 2020, 2024). Indeed, the most luminous SLSNeII show no early-time evidence for narrow lines (e.g., S. Gezari et al. 2009; A. A. Miller et al. 2009), supporting a configuration in which the CSM shock is initially embedded behind the photosphere. Additionally, a fraction of SLSNeII show no narrow lines during the photospheric phase (C. Inserra et al. 2018; T. Kangas et al. 2022).

Figure 9 provides a schematic depiction of the envisioned shock interaction. The SN ejecta collides with a CSM disk, starting at its inner edge, forming forward shocks (FSs) and reverse shocks (RSs), sandwiched between a swept-up shell of

[10] For red supergiants, their massive thick envelopes prevent a jet from breaking out of the stellar surface and producing high-energy emission akin to typical long gamma-ray bursts (e.g., C. D. Matzner 2003; T. Matsumoto et al. 2015; but also see E. Quataert & D. Kasen 2012 for the case of very-long-duration events).

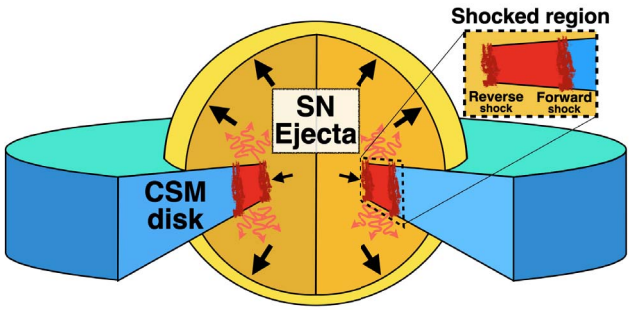

Figure 9. A schematic diagram of the envisioned scenario for shock interaction between the SN ejecta and an equatorial CSM disk. The radiation released by the ejecta–CSM shocks in the equatorial regions provides a source of internal (subphotospheric) heating for the bulk of the faster, effectively freely expanding ejecta at higher latitudes.

shocked gas, which expands outward in time. Since the portion of the SN ejecta directed along the polar region expands relatively freely, without encountering significant mass, it can envelope the slower-expanding shocked region (e.g., B. D. Metzger 2010; J. E. Andrews & N. Smith 2018). Radiation generated at the equatorial shock thus diffuses vertically into the ejecta, serving as an effective internal heating source for a (one-dimensional) SN light-curve model (e.g., B. D. Metzger & O. Pejcha 2017). We assume that the shocked CSM expands only in the radial direction, retaining its initial solid angle. We also neglect the finite time required for radiation to diffuse radially out of the disk and into the surrounding SN ejecta; our model thus provides a maximal heating luminosity and hence a conservative upper limit on the corresponding heating-extended plateau duration.

We adopt a radial density profile for the equatorial disk corresponding to that of a steady wind:

$$\rho_{\rm CSM} = \frac{\dot{M}}{4\pi f_\Omega v_{\rm CSM} r^2}, \tag{68}$$

where $f_\Omega < 1$ is the fraction of the total solid angle subtended by the disk, $v_{\rm CSM}$ is the CSM radial velocity, and $\dot{M}$ is the wind mass-loss rate. We estimate the effective heating rate due to CSM shock interaction as follows (a more detailed description of the shock evolution, for a generic density profile index, is given in Appendix C). The time evolution of the shocked region can be described by mass and momentum conservation (e.g., B. D. Metzger & O. Pejcha 2017). We assume a sufficiently dense CSM such that both FSs and RSs are radiative. Since the radial width of the shocked region is small in this case, we characterize the shell of shocked gas by a representative radius $R_{\rm sh}$ and velocity $v_{\rm sh}$.

Initially, the shock expands outward at a roughly constant speed close to that of the SN ejecta, the swept-up mass growing as $M_{\rm sh} \simeq \dot{M} v t / v_{\rm CSM}$. Once $M_{\rm sh}$ becomes comparable to the shocked ejecta mass, $f_\Omega M$, the shell of shocked gas starts to appreciably decelerate, on a characteristic timescale

$$t_{\rm dec} \simeq \frac{f_\Omega M v_{\rm CSM}}{\dot{M} v} \simeq 610\,{\rm day}\,\frac{f_{\Omega,-1} M_{10} v_{\rm CSM,100}}{v_{6000}\dot{M}_{-2}^{-1}}, \tag{69}$$

where $v_{\rm CSM} = 100\,v_{\rm CSM,100}\,{\rm km\,s^{-1}}$, $\dot{M} = 10^{-2}\dot{M}_{-2}\,{\rm M_\odot\,yr^{-1}}$, and $f_\Omega = 0.1 f_{\Omega,-1}$. From momentum conservation, the radius and velocity of the shell evolve according to

$$R_{\rm sh} \simeq \begin{cases} vt & :t < t_{\rm dec}, \\ v t_{\rm dec}\left(\dfrac{t}{t_{\rm dec}}\right)^{1/2} & :t > t_{\rm dec}, \end{cases} \tag{70}$$

$$v_{\rm sh} \simeq \begin{cases} v & :t < t_{\rm dec}, \\ v\left(\dfrac{t}{t_{\rm dec}}\right)^{-1/2} & :t > t_{\rm dec}. \end{cases} \tag{71}$$

The kinetic luminosity of the FS dominates that of the RS, and thus the FS dominates the ejecta heating. The FS luminosity evolves according to

$$H(t) \sim 4\pi f_\Omega R_{\rm sh}^2 \rho_{\rm CSM} v_{\rm sh}^3 = \frac{\dot{M} v_{\rm sh}^3}{v_{\rm CSM}} \tag{72}$$

$$\simeq 1.4 \times 10^{43}\,{\rm erg\,s^{-1}}\,\frac{v_{6000}^3 \dot{M}_{-2}}{v_{\rm CSM,100}} \begin{cases} 1 & :t < t_{\rm dec}, \\ \left(\dfrac{t}{t_{\rm dec}}\right)^{-\frac{3}{2}} & :t > t_{\rm dec}. \end{cases}$$

Interestingly, then, for a wind-like CSM profile $\rho_{\rm CSM} \propto r^{-2}$, the heating-rate evolution again follows the functional form of Equation (54).

Our treatment of the shock as an internal heating source requires the shocked region to remain inside the SN photosphere, i.e.,

$$R_{\rm sh} \leqslant R_{\rm ph} (= xR). \tag{73}$$

After this condition becomes violated, we truncate the heating rate in our model, i.e., $H = 0$ for $R_{\rm sh} > R_{\rm ph}$.

Figure 10 shows light curves, as well as the evolution of the photosphere radius and velocity, for various assumed CSM wind mass-loss rates, obtained by calculating the shock evolution numerically (see Appendix C for the exact equations). The inner edge of the CSM disk is assumed to coincide with the progenitor star radius, and we fix the other CSM properties according to $f_\Omega = 0.1$ and $v_{\rm CSM} = 100\,{\rm km\,s^{-1}}$ (the results depend only on the overall CSM density normalization $\propto \dot{M}/v_{\rm CSM}$, provided that $v_{\rm CSM} \ll v_{\rm sh}$). As a general rule, the ejecta cannot be appreciably accelerated as a result of CSM interaction, because the ultimate source of the ejecta heating is the initial kinetic energy of the ejecta that intercepts the CSM, $\sim f_\Omega E_{\rm kin,0}$.

While the lengthening of the plateau phase from shock heating is typically only moderate, we identify an "optimal" pre-explosion progenitor mass-loss rate, $\dot{M} \sim 0.1\,M_\odot\,{\rm yr^{-1}}$ (for $v_{\rm CSM} = 100$ km s^{-1}), which maximizes the plateau duration. While the shock power increases for larger $\dot{M}$, the duration of this heating phase is correspondingly shorter, because of the shorter deceleration time, which results in a lower shock luminosity during the recombination phase. On the other hand, for less massive CSM (smaller $\dot{M}$), the shock heating is sustained for a longer timescale, but at a value too low to sustain the ejecta ionization and appreciably lengthen the plateau. The shocked region also emerges faster from the photosphere in the freely coasting case, violating the condition of Equation (73) and terminating the ejecta heating.

The above description of the optimal mass-loss rate is supported by Figure 11, which again shows the key timescales, this time as a function of $\dot{M}$. For $\dot{M} \gtrsim 0.1\,M_\odot\,{\rm yr^{-1}}$, the

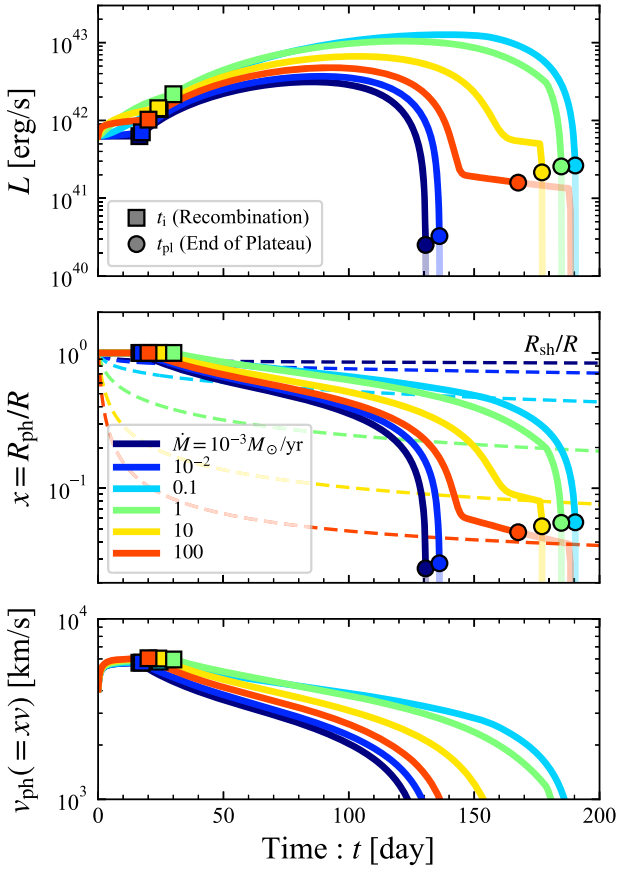

Figure 10. The same as Figure 5 but for energy injection due to the shock interaction between the SN ejecta and a disk-like CSM. For the CSM velocity and solid angle covering fraction, we adopt $v_{\rm CSM} = 100$ km s^{-1} and $f_\Omega = 0.1$, respectively. In the middle panel, the dashed curves show the shock radius in units of the ejecta radius, $R_{\rm sh}/R$. Once the shocks emerge from the photosphere such that $R_{\rm sh} > R_{\rm ph}$ (the intersection of the solid and dashed curves), the shock can no longer supply a source of internal heating to the ejecta and internal heating is truncated. This truncation can best be seen with the yellow line ($\dot{M} = 10 M_\odot {\rm yr}^{-1}$).

deceleration of the ejecta is significant during the recombination phase (right of the dashed line), and the resulting weaker shock power, $L_{\rm sh} \propto \dot{M}^{-1/2}$, causes the plateau duration to shorten. For $\dot{M} \lesssim 0.1\, M_\odot$ yr^{-1}, the shock does not experience significant deceleration during the recombination phase and eventually overtakes the photosphere. The small rise in the plateau duration around $\dot{M} \sim 10 - 100\, M_\odot$ yr^{-1} is caused by the tail of the light curve tracing the shock luminosity, as shown in Figure 10. In summary, the optimal mass-loss rate for lengthening the plateau duration is that for which ejecta deceleration and recombination occur simultaneously. However, even in this optimal case, the plateau duration is extended by only a factor of $\sim$2 compared to the no-heating case. In Appendix C, we show this conclusion also holds for generic (i.e., non-wind-like) CSM density profiles.

It is not straightforward to estimate analytically the optimal $t_{\rm pl}$-maximizing mass-loss rate, because the effects of shock heating on the recombination process are subtle for $\dot{M} \sim 10^{-2}$–$10^{-1}\, M_\odot$ yr^{-1}. As an alternative, we adopt the mass-loss rate above which the resulting shock heating appreciably slows the ejecta recombination (the analog of $H_{\rm cr}$ from the constant-heating-rate case). Equating Equations (12)

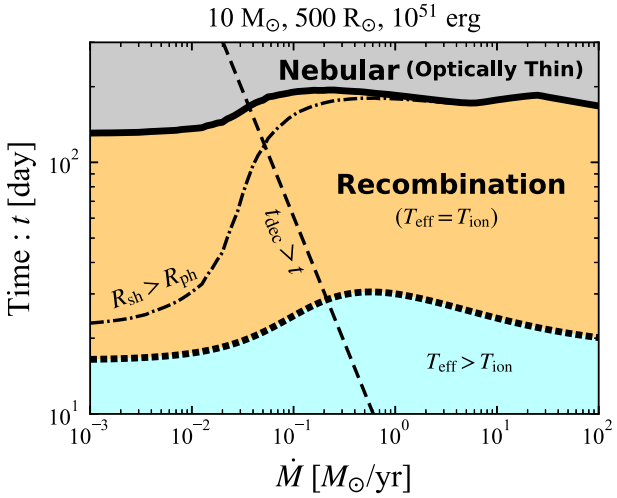

Figure 11. The same as Figure 2 but for shock interaction heating for different normalizations of the wind-like CSM density profile. The dashed diagonal lines denote the deceleration timescale before which the shock expands freely and the shock luminosity is approximately constant. The dashed–dotted line shows the time at which the shock radius becomes larger than the retreating SN photosphere.

with (72) ($t < t_{\rm dec}$), we find

$$\dot{M}_{\rm cr} \simeq 3.4 \times 10^{-2}\, M_\odot\ {\rm yr}^{-1}\, M_{10}\, v_{6000}^{-2}\, v_{\rm CSM,100} \left(\frac{\zeta}{0.83}\right)^{-3}. \quad (74)$$

Here, we have written $v_{\rm sh} = \zeta v$ to account for the moderate deceleration of the ejecta even prior to the formal deceleration time, where $\zeta \simeq 0.83$ is motivated by our numerical results. This estimate slightly underestimates the true $\dot{M}$ that maximizes $t_{\rm pl}$ in our full numerical calculations (Figure 11).

5. Discussion

Figure 12 summarizes the allowed space of light-curve properties for the wide range of heating sources considered in this paper, for fiducial progenitor star/explosion properties. The presence of a sustained heating source generally acts to boost the plateau luminosity and duration above those of the no-heating case (the latter of which describes most SNeIIP, shown for comparison with the brown crosses). While increases in the luminosity of up to several orders of magnitude are possible for sufficiently powerful heating rates, the corresponding boost to the plateau duration is more tightly bounded, to within a factor $\lesssim$3 of the duration in the zero-heating case. The attainable plateau duration is capped by the limiting constant-heating-rate case (depicted as the thick red curve). This maximal duration is approximately given by Equation (46), which, expressed in terms of ejecta mass and explosion energy, gives

$$t_{\rm pl,max} \simeq 580\ {\rm day}\ T_{\rm i,6000}^{-2/3} M_{10}^{17/24} E_{0,51}^{-7/24}. \quad (75)$$

Figure 12 also shows for comparison a sample of Type IIn SNe, i.e., those showing narrow hydrogen lines indicative of CSM interaction, including the outlier event SN 2016aps. We also show two other "extreme" explosions: iPTF14hls (I. Arcavi et al. 2017) and AT 2021lwx (B. M. Subrayan et al. 2023; P. Wiseman et al. 2023), though the latter has been interpreted as a tidal disruption event by some authors.

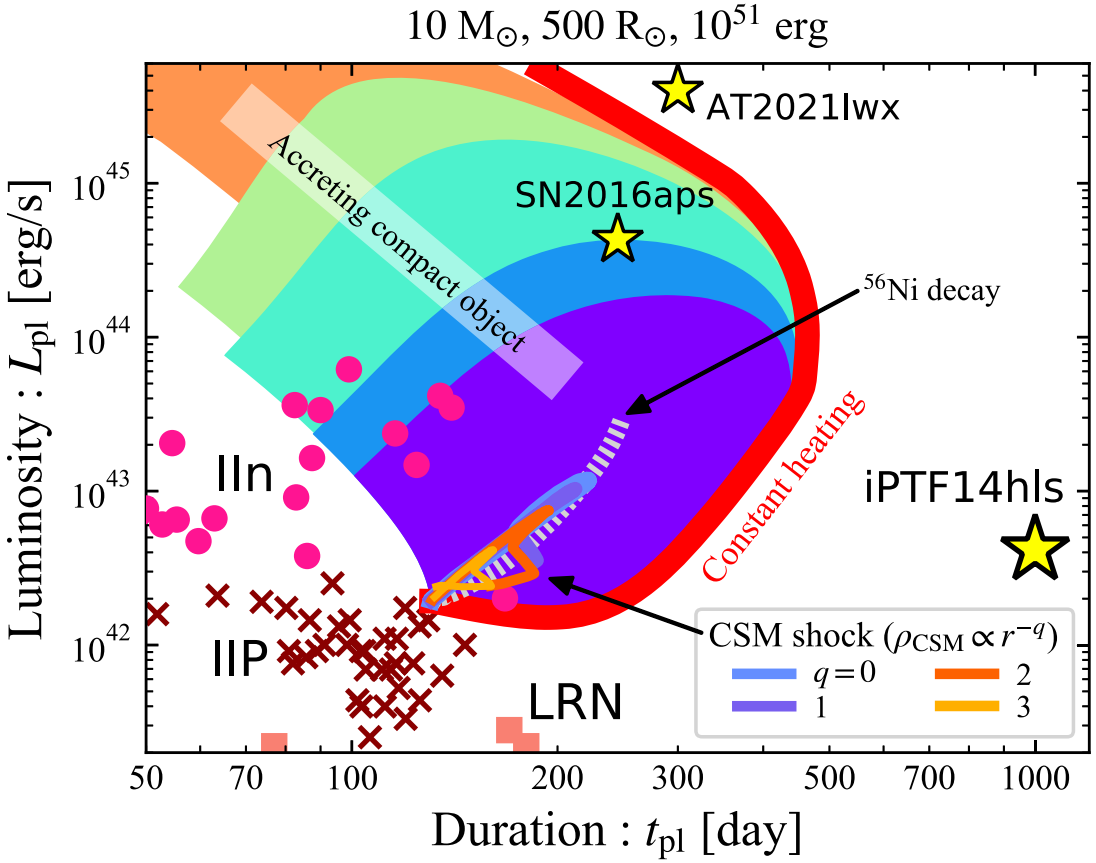

Figure 12. The allowed space of plateau duration and luminosity for different heating sources. The colored shaded regions correspond to an accreting compact object (see Figures 3 and 8), bounded by a solid red curve corresponding to the constant-heating-rate case. The gray dashed and colored solid curves denote, respectively, radioactive ^{56}Ni heating and CSM shock interaction (for a range of different radial density profiles). The ranges of nickel masses and CSM density normalizations follow those in Figures 6 and 15, respectively. The brown crosses, magenta circles, and orange squares show the parameters for SNeIIP, Type IIn SNe, and LRNe (data are taken from A. Nyholm et al. 2020, L. Martinez et al. 2022a, and T. Matsumoto & B. D. Metzger 2022b). Three stars represent peculiar events: iPTF14hls (I. Arcavi et al. 2017; J. E. Andrews & N. Smith 2018), SN 2016aps (M. Nicholl et al. 2020), and AT 2021lwx (B. M. Subrayan et al. 2023; P. Wiseman et al. 2023). For Type IIn SNe, SN 2016aps, and AT 2021lwx, we use peak luminosities and show durations corresponding to the timescale over which the light curve remains within $\lesssim$1 mag of the peak.

5.1. Minimum Ejecta Mass of Long-plateau Transients

The existence of a maximal plateau duration implies that a minimum ejecta mass is required to realize the plateau duration of a given observed event. Since the duration–luminosity trajectory for the limiting constant-heating-rate case depends on the ejecta properties (bottom panel of Figure 3), we show in the top panel of Figure 13 these curves for an expanded parameter range of initial explosion energies 10^{50} erg to 10^{53} erg (the thin to thick curves) and ejecta masses from 1 to $10^3\,M_\odot$ in steps of 0.2 dex.[11] As expected from Section 3, the maximal plateau duration increases with ejecta mass and decreases with higher explosion energy.

The bottom panel of Figure 13 depicts the minimum ejecta mass, $M_{\rm min}$, needed to produce a given plateau duration. Based on the $L_{\rm pl}-t_{\rm pl}$ trajectory (Equation (53), for the $H < H_{\rm pl,max}$ case), we estimate

$$M_{\rm min} \simeq 180\,M_\odot\,E_{0,52}^{3/5}\left(\frac{L_{\rm pl}}{3\times10^{42}\,{\rm erg\,s^{-1}}}\right)^{-1/5}\left(\frac{t_{\rm pl}}{10^3\,{\rm day}}\right)^{6/5}, \quad (76)$$

in rough agreement with the full calculation. If the ejecta velocity can be measured observationally, the explosion energy and hence $M_{\rm min}$ can be more robustly constrained. Along each curve, a small circle denotes the minimum explosion energy in shock-powered scenarios, $E_0 \gtrsim t_{\rm pl}L_{\rm pl}/f_\Omega$, which is consistent with generating the radiated energy.

As expected from the $L_{\rm pl}-t_{\rm pl}$ trajectories, the curves of $M_{\rm min}$ terminate at high energies (e.g., at $E_0 \simeq 10^{52}$ erg for $L_{\rm pl}=10^{43}\,{\rm erg\,s^{-1}}$ and $t_{\rm pl}=300$ days) and flatten for lower energy (e.g., $E_0 \lesssim 10^{51}$ erg for $L_{\rm pl}=10^{43}\,{\rm erg\,s^{-1}}$ and $t_{\rm pl}=1000$ days). The former behavior occurs because the $L_{\rm pl}-t_{\rm pl}$ trajectory rises with increasing E_0 until it no longer touches the given $L_{\rm pl}$. The flattening at low E_0 occurs because at high heating rates $H \gtrsim H_{\rm pl,max}$, the $L_{\rm pl}-t_{\rm pl}$ trajectory loses sensitivity to the initial explosion energy (Equation (53) for the $H > H_{\rm pl,max}$ cases). This flattening occurs once the ejecta experiences significant acceleration, leading to a breakdown of the relations $E_0 = 3Mv^2/20$, $E_{\rm kin,0}=E_0$, and $v=\sqrt{2}\,v_0$ (Equations (7)). The contours of constant ejecta velocity are denoted by the gray dashed diagonal lines in the bottom panel of Figure 13.

As an example, we show the $M_{\rm min}$ trajectory for iPTF14hls ($t_{\rm pl}\sim10^3$ days; $L_{\rm pl}\simeq3\times10^{42}\,{\rm erg\,s^{-1}}$) as a red dashed line in the bottom panel of Figure 13 (along this line, acceleration of

[11] We remove models satisfying $E_0=10^{50}$ erg and $M\gtrsim400\,M_\odot$, because gas pressure dominates over radiation pressure in the ejecta for these parameters, violating our assumption (Equation (14)).

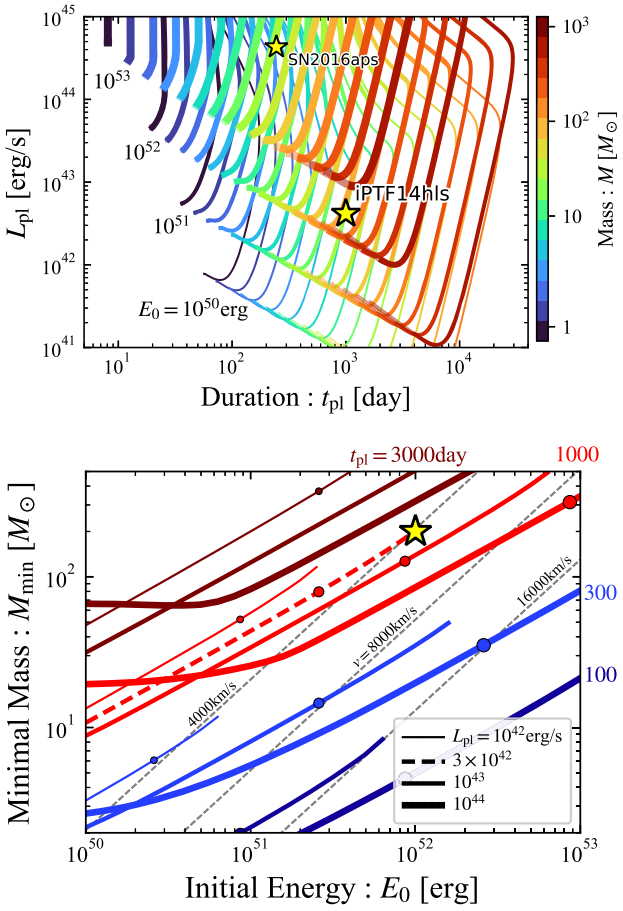

Figure 13. Top: trajectories of plateau duration and luminosity for the bounding constant-heating-rate case ($H = $ const), similar to Figure 3 but now for a range of energies $E_0 = 10^{50}$– 10^{53} erg and ejecta masses $M = 1$–$10^3\,M_\odot$, as labeled. The range of heating-rate values H along each trajectory is set to cover $H_{\rm min}$ (Equation (35)), so that the heating-free solutions are present for each parameter set. On each trajectory, a segment violating the one-zone condition (Equation (A1)) is shown by a transparent line. Bottom: minimal ejecta mass $M_{\rm min}$ for producing a given plateau duration (different colored lines) and luminosity (different line styles) as a function of the initial explosion energies E_0. The gray dashed lines show the corresponding mean ejecta velocity. Along each curve, a circle denotes the minimum energy in shock interaction scenarios, $E_0 \gtrsim t_{\rm pl}L_{\rm pl}/f_\Omega$. A star represents the location of iPTF14hls with $t_{\rm pl} \simeq 10^3$ days, $L_{\rm pl} \simeq 3\times10^{42}$ erg s^{-1}, and $v \simeq 4000$ km s^{-1}.

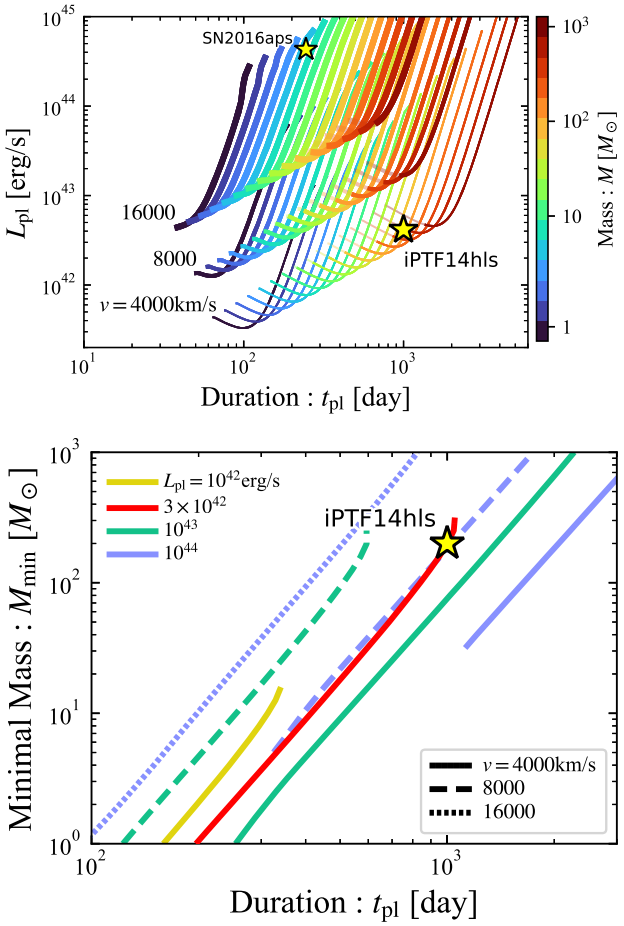

Figure 14. Top: the same as the top panel of Figure 13 but for fixed v. The trajectories terminate at high luminosity (roughly corresponding to $H_{\rm pl,max}$, where the ejecta accelerates). Bottom: minimal ejecta mass $M_{\rm min}$ for producing a given plateau duration $t_{\rm pl}$ for different luminosity and velocity.

the ejecta is negligible). If the velocity obtained from the Fe-line absorption minimum, $v \simeq 4000\,{\rm km\,s^{-1}}$ (I. Arcavi et al. 2017), is representative of the unshocked ejecta, then we find the initial explosion energy and ejecta mass are constrained to be $E_0 \simeq 10^{52}$ erg and $M_{\rm ej} \gtrsim M_{\rm min} \simeq 200\,M_\odot$, respectively. Such a large ejecta mass would obviously require a very massive progenitor star, possibly supporting a pulsational PI explanation for this event (e.g., S. E. Woosley et al. 2007; S. E. Woosley 2018; L.-J. Wang et al. 2022; S. E. Woosley & N. Smith 2022; K.-J. Chen et al. 2023).

The minimum ejecta mass (Equation (76)) can be expressed in terms of v instead of E_0:

$$M_{\rm min} \simeq 140\,M_\odot \left(\frac{L_{\rm pl}}{3\times10^{42}\,{\rm erg\,s^{-1}}}\right)^{-1/2} \left(\frac{v}{4000\,{\rm km\,s^{-1}}}\right)^3 \left(\frac{t_{\rm pl}}{10^3\,{\rm day}}\right)^3, \quad (77)$$

where again acceleration of the ejecta is neglected. The bottom panel of Figure 14 shows $M_{\rm min}$ as a function of the plateau duration for different values of $L_{\rm pl}$ and v. Each $M_{\rm min}$ curve terminates at both short and long plateau durations, the latter corresponding to the regime of appreciable acceleration of the ejecta ($H \gtrsim H_{\rm pl,max}$). This is illustrated in the top panel of Figure 14, which is similar to Figure 13 but shows $L_{\rm pl} - t_{\rm pl}$ trajectories for different assumed mean ejecta velocities.

The above demonstrates a methodology for placing lower limits on the ejecta mass for given SNe. This can help identify the explosions of very massive stars, including PISNe caused by pair-production-induced collapse leading to explosive oxygen burning for progenitors with $\simeq$140–260 $M_\odot$ (Z. Barkat et al. 1967; G. Rakavy & G. Shaviv 1967; A. Heger & S. E. Woosley 2002; A. Heger et al. 2003; D. Kasen et al. 2011; L. Dessart et al. 2013; K.-J. Chen et al. 2014a; A. Kozyreva et al. 2014a, 2014b; M. S. Gilmer et al. 2017) and general-relativistic instability SNe (GRSNe) for supermassive Population III stars $\sim 10^{4-5}\,M_\odot$ (S. Chandrasekhar 1964; G. M. Fuller et al. 1986; P. J. Montero et al. 2012; K.-J. Chen et al. 2014b; T. Matsumoto et al. 2016; H. Uchida et al. 2017; C. Nagele et al. 2020, 2022; T. J. Moriya et al. 2021a). These explosions should be rare and current observations only weakly constrain their rates. For instance, T. J. Moriya et al. (2021b) constrain the rate of long-lasting H-rich SNe observationally, finding

$\sim$40% of Type IIn exhibit light curves lasting longer than a year, while the rate of PISNe is constrained to $\lesssim 0.01\%-0.1\%$ of the total core-collapse SNe rate. More recently, using JWST observations, T. J. Moriya et al. (2023) constrain the rate of GRSNe to $\lesssim 800\,\mathrm{Gpc^{-3}\,yr^{-1}}$. With current and upcoming facilities such as JWST, Rubin, Euclid, and Roman in an excellent position to discover additional candidate explosions in the near future, our framework may prove useful in helping to identify these events and constraining the ejecta properties.

5.2. Application to Luminous Red Novae

Luminous red novae (LRNe) are weeks- to months-long transients with luminosities between those of classical novae and SNe (e.g., H. E. Bond et al. 2003; R. Tylenda et al. 2011; N. Blagorodnova et al. 2017), which are believed to arise from stellar mergers (R. Tylenda & N. Soker 2006; N. Ivanova et al. 2013). While dimmer members of the LRN class with $\lesssim 10^{40}\,\mathrm{erg\,s^{-1}}$ can be powered exclusively by hydrogen recombination energy, the brightest and longest events may require an additional energy source (T. Matsumoto & B. D. Metzger 2022b), most likely shock interaction between the merger ejecta and stellar material unbound from the binary prior to the dynamical merger (e.g., O. Pejcha et al. 2016a, 2016b; B. D. Metzger & O. Pejcha 2017; M. MacLeod & A. Loeb 2020a).

Our results illustrate that shock interaction can increase the plateau duration and luminosity by at most a factor of $\sim$2 and $\sim$10, respectively, boosting the radiated energy by a factor $\lesssim$20 compared to the zero-heating case. Scaling to properties typical of stellar mergers, the duration, luminosity, and radiated energy in the zero-heating case are estimated by Equations (17), (19), and (18):[12]

$$t_{\rm pl,Popov} \simeq 78\ \mathrm{day}\left(\frac{M}{3\,M_\odot}\right)^{5/14}\left(\frac{v}{10^3\,\mathrm{km\,s^{-1}}}\right)^{-5/14}\left(\frac{R_0}{30\,R_\odot}\right)^{1/7}, \tag{78}$$

$$L_{\rm pl,Popov} \simeq 2.6\times 10^{40}\,\mathrm{erg\,s^{-1}}\left(\frac{M}{3\,M_\odot}\right)^{3/7}\left(\frac{v}{10^3\,\mathrm{km\,s^{-1}}}\right)^{11/7}\left(\frac{R_0}{30\,R_\odot}\right)^{4/7}, \tag{79}$$

$$E_{\rm pl,Popov} \simeq 1.7\times 10^{47}\,\mathrm{erg}\left(\frac{M}{3\,M_\odot}\right)^{11/14}\left(\frac{v}{10^3\,\mathrm{km\,s^{-1}}}\right)^{17/14}\left(\frac{R_0}{30\,R_\odot}\right)^{5/7}. \tag{80}$$

While these estimates fall short of explaining the most luminous LRNe by an order of magnitude for reasonable ejecta masses (T. Matsumoto & B. D. Metzger 2022b), the presence of CSM interaction could alleviate these tensions by boosting the plateau luminosity and duration for optimally chosen values of the (pre-merger) binary mass-loss rate, $\dot{M}\sim\dot{M}_{\rm cr}$ (Section 4.4). In particular, from Equation (74) we find

$$\dot{M}_{\rm cr} \simeq 1.34\,\mathrm{M_\odot\,yr^{-1}}\left(\frac{M}{3\,M_\odot}\right)\left(\frac{v}{10^3\,\mathrm{km\,s^{-1}}}\right)^{-2} v_{\rm CSM,100}\left(\frac{\zeta}{0.56}\right)^{-3}, \tag{81}$$

where here we take $\zeta\equiv v_{\rm sh}/v\simeq 0.56$, appropriate for LRN parameters. Since mass loss prior to the merger (e.g., from the binary L2 Lagrange point) typically amounts to at most tens of percent of the donor star's mass (M. MacLeod et al. 2017; O. Pejcha et al. 2017; M. MacLeod & A. Loeb 2020b), this optimal mass-loss rate could be realized in a massive $\sim 10\,M_\odot$ binary that loses $\sim M_\odot$ over the year preceding the dynamical merger event.

6. Summary and Conclusions

The basic observables of SNeIIP contain information on the properties of the exploding star, which must be understood to take advantage of the growing samples of SNe to be discovered, e.g., by Rubin, JWST, and Roman. One such readily measured property is the duration of the optically thick plateau phase, which canonically depends (for a given explosion energy and progenitor radius) on the ejecta mass. All else being equal, a longer plateau requires a higher ejecta mass and hence a more massive progenitor star. However, the plateau duration can also be prolonged by the presence of a sustained internal heating source, which keeps the ejecta ionized—and hence optically thick—longer than in a passively cooling case. Indeed, growing evidence points to additional heating sources being required to power a large number of peculiar SNe and related optical transients.

To understand the interplay between these processes, and how to break the degeneracies to better constrain the ejecta properties of individual events, we have studied the effects of an internal heating source on the light curves of hydrogen-rich explosions by generalizing the analytical SNIIP light-curve model of D. V. Popov (1993). Our findings are summarized as follows:

1. While sufficiently large internal heating rates can boost the plateau luminosity by several orders of magnitude, the plateau duration can be prolonged by at most a factor of $\sim$2–3 times compared to the zero-heating case. For a temporally constant heating source, the maximal plateau duration is realized for the maximal heating rate that does not appreciably alter the ejecta dynamics. Above this critical heating rate, the ejecta experiences significant acceleration, reducing the photon diffusion timescale and hence shortening the plateau.
2. Heating from ^{56}Ni decay is found to boost the plateau duration by at most a few tens of percent for the nickel masses typical of SNeIIP, consistent with previous findings in the literature. This agreement with more sophisticated radiation transport calculations supports our model capturing at least semi-quantitatively the effects of an internal heating source on SN light curves.

[12] Note that for these parameters, the ejecta energy,

$$E_0 \simeq 9.0\times 10^{48}\,\mathrm{erg}\left(\frac{M}{3\,M_\odot}\right)\left(\frac{v}{10^3\,\mathrm{km\,s^{-1}}}\right)^2,$$

is close to the limit below which gas pressure is comparable to radiation pressure (Equation (14)).

3. Insofar that sustained energy injection from a central engine, such as a millisecond magnetar or accreting compact object, can be described as heating with a characteristic duration and total deposited energy, as in Equations (63) or (66), the resulting SN plateau phase can exhibit a wide range of luminosities and durations depending on these parameters. While a longer engine-heating timescale (e.g., the magnetar spindown time $t_{\rm sd}$ or the mass fallback timescale $t_{\rm fb}$) results in a longer plateau duration, the latter is again capped at a few times the duration in the zero-heating case in the limit of temporally constant heating ($t_{\rm sd}$, $t_{\rm fb} \to \infty$).
4. Shock interaction between the fast SN ejecta and slower equatorially confined ("disk-like") CSM can provide an additional source of subphotospheric heating for sustaining a longer plateau (Figure 9). However, for typical parameters, shock heating can boost the plateau duration by at most a factor of $\sim$2 for an optimal mass-loss rate (Equation (74)). While a very massive CSM results in a high shock luminosity, the concomitant strong deceleration of the ejecta limits this phase to early times. By contrast, while the ejecta deceleration is weaker for low CSM masses, in that case the shocks quickly expand beyond the retreating photosphere radius, therefore no longer serving as a sustained internal heating source capable of keeping the ejecta ionized.

Our results are conveniently summarized in the space of plateau duration and luminosity, as shown in Figure 12 and compared to observed hydrogen-rich SNe.

1. Motivated by our finding that the temporally constant heating case defines an absolute boundary on the attainable duration and luminosity, we developed a framework to constrain the minimal mass for observed events, as captured in Equation (77) in Section 5.1. As a proof of principle, we used the observed duration, luminosity, and ejecta velocity to constrain the ejecta mass in iPTF14hls to $\gtrsim 200\,M_\odot$, supporting an explosion of a very massive star, such as a PISN.
2. Our results can also be applied to shock interaction heating in LRNe from stellar mergers. We confirmed that the shock interaction between the LRN ejecta and circumbinary material ejected prior to the merger can indeed explain the otherwise puzzling properties of the most luminous events, for an assumed pre-dynamical binary mass-loss rate of $\sim M_\odot\,{\rm yr}^{-1}$.

Acknowledgments

T.M. acknowledges support from the JSPS Overseas Research Fellowship, the Hakubi project at Kyoto University, and JSPS KAKENHI (grant No. 24K17088). B.D.M. acknowledges support from the National Science Foundation (grant No. AST-2009255). The Flatiron Institute is supported by the Simons Foundation.

Appendix A
Validation of the One-zone Model

Here, we discuss the validity of the one-zone model employed in our study. As briefly discussed in Section 2, the original works by W. D. Arnett (1980) and D. V. Popov (1993) did not take the one-zone approach but derived the radial distribution of temperature by solving the diffusion equation. We nevertheless found their light-curve predictions to be reasonably reproduced by the one-zone model. This may partly result from the fact that the W. D. Arnett (1980) temperature profile is relatively flat, being described by a Bessel-type function, $T^4 \propto \sin(r)/r$.

We first reconsider the original model by W. D. Arnett (1980) and D. V. Popov (1993). One of the key assumptions of their solution is that the temperature profile exhibits a self-similar profile, which is not always a good approximation, particularly at early times. A self-similar profile is established not instantaneously but instead gradually, over a timescale of $\sim t_{\rm diff}$, as can be seen in simulations by, e.g., D. K. Khatami & D. N. Kasen (2019). However, in the case of SNeIIP, the (initial) temperature profile is set not by radiative diffusion from the inner region, but by heating from the SN shock. As shown in previous studies (e.g., M. C. Bersten et al. 2011; J. A. Goldberg et al. 2019), the resulting radial profile exhibits a relatively flat shape, due to the nature of the shock heating, which could be nicely approximated by the self-similar solution of W. D. Arnett (1980) and the one-zone model. Furthermore, this flat temperature profile does not evolve significantly with time, its normalization just being reduced by adiabatic cooling, until a diffusion wave or recombination front reaches each layer.

The situation becomes more complex when a heating source is present within the ejecta. As discussed in Section 4, this heating may be spatially concentrated, which challenges the one-zone approach. An ultimate validation will require detailed radiation hydrodynamical simulations, but there are several reasons why the one-zone model employed in this study could still be justified to first order. In SNeIIP, the diffusion timescale is already comparable to the plateau duration without heating (see Equations (4) and (17)) for typical parameter values. Since our main focus is on quantifying how the plateau duration can be extended by a heating source, the diffusion timescale is thus almost always shorter than the (lengthened) plateau duration. Thus, the effects of radiative diffusion are likely to already begin during the recombination phase, bringing most of the ejecta into causal contact and thus justifying a single-zone approach. In cases where the external energy source is strong enough to affect the ejecta dynamics, the one-zone description becomes more applicable. This is because, while in our model we treat the ejecta acceleration as being driven exclusively by internal pressure (see Equation (6)), a portion of this acceleration will occur as the result of a shock for dynamically relevant heating rates. In particular, if radiative diffusion cannot transport the energy being deposited by the external source, it will accumulate around the location where it is deposited, eventually driving a shock wave, which propagates outward, both heating and accelerating the ejecta. Similar to the above argument regarding normal SNeIIP (heated by the initial SN shock), such an external-heating-induced shock will also establish a relatively flat temperature profile, which again can be described reasonably well by the one-zone model. The shock-driven acceleration may furthermore trigger the Rayleigh–Taylor instability (see, e.g., A. Suzuki & K. Maeda 2021), which mixes and homogenizes the ejecta.

The above arguments hold only for SNeIIP and less massive transients, such as LRNe. However, for explosions with more massive ejecta, the diffusion timescale can be longer than the plateau duration obtained by our model, invalidating the one-

zone approach. For a given heating luminosity, the critical mass above which the diffusion time becomes longer than the plateau duration is given by comparing Equations (4) and (33):

$$M_{\times} \simeq 8300\, M_{\odot}\, v_{6000}^{-3} T_{\rm i,6000}^{-4} H_{43}. \tag{A1}$$

While large compared to typical stellar masses, this limit should be kept in mind when carrying out broad parameter studies. In fact, for our calculations presented in Section 5, this condition is violated for the highest-ejecta-mass cases, which we therefore mark with transparent lines in Figures 13 and 14.

Appendix B
Analytic Estimates for Broken-power-law Heating Profile

We now extend our analytic estimates from Section 3 for a constant heating rate to the broken-power-law heating rate of the form of Equation (54). We first consider cases in which the heating affects only the thermal evolution of ejecta, as in Section 3.1. A quantitatively different evolution from the $H=$ const case occurs for $t_{\rm br} < t < t_{\rm i}$. In this regime, as long as $\alpha < 2$, the internal energy grows as $E \simeq tH \propto t^{1-\alpha}$ after the deposited energy has become comparable to the internal energy at the time

$$\tilde{t}_{\rm h} = \left(\frac{t_{\rm h}}{t_{\rm br}}\right)^{\frac{\alpha}{2-\alpha}} t_{\rm h}, \tag{B1}$$

where the definition for $t_{\rm h}$ follows Equation (24) but now for $H \to \widetilde{H}$. The evolutions of the internal energy and effective temperature subsequently obey

$$E \simeq \left(\frac{t}{t_{\rm br}}\right)^{1-\alpha} \widetilde{H} t_{\rm br}, \tag{B2}$$

$$T_{\rm eff} \simeq \left(\frac{\widetilde{H}}{H_{\rm cr}}\right)^{1/4} \left(\frac{t}{t_{\rm br}}\right)^{-\alpha/4} T_{\rm i}, \tag{B3}$$

respectively. For sufficiently high heating rates, $\widetilde{H} > H_{\rm cr}$, recombination begins at the time

$$\tilde{t}_{\rm i} = \left(\frac{\widetilde{H}}{H_{\rm cr}}\right)^{1/\alpha} t_{\rm br}. \tag{B4}$$

When $\alpha \geqslant 2$, the evolution until recombination completes is identical to the zero-heating case.

From Equation (B1) we find that for heating rates smaller than a critical rate, $\widetilde{H} < t_0 E_0 / t_{\rm br}^2$, the thermal evolution of the ejecta is affected only after the heating rate has begun to decline ($\tilde{t}_{\rm h} > t_{\rm br}$). For higher heating rates, the evolution is modified before the heating breaks ($t_{\rm h} < t_{\rm br}$), and for $\alpha < 2$ it is identical to the $H=$ const case until $t < t_{\rm br}$. The evolution at $t > t_{\rm br}$ is identical to that given in Equations (B2) and (B3). For $\alpha \geqslant 2$, the internal energy is effectively reset by the injected heat at the time $t_{\rm br}$, such that $E \simeq \widetilde{H} t_{\rm br} (t/t_{\rm br})^{-1}$. And the effective temperature and recombination time follow the same expressions as in Equations (27) and (28) for the regimes of $t_{\rm diff} < t$ and $H_{\rm cr} < H$, respectively, but making the replacements $t_{\rm diff} \to t_{\rm br}$ and $H \to \widetilde{H}$.

The photosphere evolution during the recombination phase can be derived following similar arguments as in the constant-heating case. In particular, when the heating rate declines before recombination begins ($t_{\rm br} < t_{\rm i}$), the photosphere location follows

$$x \simeq \begin{cases} \left(\dfrac{t}{t_{\rm i}}\right)^{-2/5} & : t < \tilde{t}_{\rm h}^{\rm rec}, \\ \left(\dfrac{\widetilde{H}}{2H_{\rm cr}}\right)^{1/4} \left(\dfrac{t}{t_{\rm br}}\right)^{-\alpha/4} & : \tilde{t}_{\rm h}^{\rm rec} < t < \tilde{t}_{\rm diff}^{\rm rec}, \\ \left(\dfrac{\widetilde{H}}{H_{\rm cr}}\right)^{1/2} \left(\dfrac{t_{\rm diff}}{t_{\rm br}}\right) \left(\dfrac{t}{t_{\rm br}}\right)^{-\frac{\alpha+2}{2}} & : \tilde{t}_{\rm diff}^{\rm rec} < t, \end{cases} \tag{B5}$$

where

$$\tilde{t}_{\rm h}^{\rm rec} = \left(\frac{\widetilde{H}}{2H_{\rm cr}}\right)^{\frac{5}{5\alpha-8}} \left(\frac{t_{\rm br}}{t_{\rm i}}\right)^{\frac{5\alpha}{5\alpha-8}} t_{\rm i}, \tag{B6}$$

$$\tilde{t}_{\rm diff}^{\rm rec} = \left(\frac{2\widetilde{H}}{H_{\rm cr}}\right)^{\frac{1}{\alpha+4}} \left(\frac{t_{\rm br}}{t_{\rm diff}}\right)^{\frac{\alpha}{\alpha+4}} t_{\rm diff}. \tag{B7}$$

Depending on the parameters, some regimes disappear; for instance, when the break in the heating rate occurs after recombination completes ($t_{\rm br} > t_{\rm i}$), the evolution follows Equation (31) until the break. However, for any set of parameters, the final regime of evolution always exists, with the condition $x\tau = 1$ again giving the plateau duration:

$$\tilde{t}_{\rm pl} \simeq \left(\frac{\widetilde{H}}{H_{\rm cr}}\right)^{\frac{1}{\alpha+6}} \left(\frac{v}{c}\right)^{\frac{1}{\alpha+6}} \left(\frac{t_{\rm br}}{t_{\rm thin}}\right)^{\frac{\alpha}{\alpha+6}} t_{\rm thin}. \tag{B8}$$

As expected, all of the expressions given here except for Equation (B4) reduce to the $H=$ const case in the limit $\alpha \to 0$.

We now discuss cases in which the heating impacts the ejecta dynamics, as considered in Section 3.2. For such large heating rates, the ejecta experiences appreciable acceleration at times $t > t_{\rm acc}$, where $t_{\rm acc}$ is again defined by Equation (38) but for $\widetilde{H}$ instead of H. While in the $H=$ const case, the acceleration was found to terminate when recombination occurs or photon diffusion becomes important, we find that acceleration can also terminate after the break in the heating rate. This is because the internal energy falls as $E \propto t^{1-\alpha}$ ($\alpha < 2$) or $\propto t^{-1}$ ($\alpha \geqslant 2$), which results in an equation of motion: $dv/dt \propto 1/(t^{\alpha} v)$ or $\propto 1/(t^2 v)$, respectively. Therefore, as long as $\alpha > 1$, as obeyed by the physically motivated heating rates we consider, the ejecta is no longer accelerated significantly after the break. This simplifies the analysis by allowing us to treat the acceleration in the same way as in the constant-heating case. In particular, we need only consider two cases, in which the ejecta acceleration terminates due to the break at $t_{\rm br}$ or photon diffusion at $t_{\rm diff}$. In the former case, the terminal velocity is given by

$$\tilde{v}_{\rm max} \simeq \left(\frac{10\widetilde{H} t_{\rm br}}{3M}\right)^{1/2}, \tag{B9}$$

and the corresponding photon diffusion timescale is given by

$$\tilde{t}_{\rm diff}^{\rm acc} = \left(\frac{27\kappa^2 M^3}{160\pi^2 c^2 t_{\rm br} \widetilde{H}}\right)^{1/4}. \tag{B10}$$

Therefore, the condition $t_{\rm br} < \tilde{t}_{\rm diff}^{\rm acc}$ is satisfied for

$$\widetilde{H} < \frac{27\kappa^2 M^3}{160\pi^2 c^2 t_{\rm br}^5}. \tag{B11}$$

The plateau duration is obtained in the same way as the $H = {\rm const}$ case—namely, by following Equation (B8)/(34), with $\tilde{v}_{\rm max}$ replacing $v_{\rm max}$ when recombination occurs after/before $t_{\rm br}$. In cases of yet stronger heating, acceleration terminates only once photon diffusion becomes important. The corresponding velocity and plateau duration in this case again follow Equations (41) and (44), respectively.

Appendix C
Details of the Ejecta–CSM Shock Dynamics

We describe our treatment of the dynamics of the shock interaction between the SN ejecta and equatorially concentrated (disk-like) CSM for the case of a generic power-law density profile (see also T. J. Moriya et al. 2013; B. D. Metzger & O. Pejcha 2017; D. Hiramatsu et al. 2024). We assume that both the FS and RS are radiative and hence both share a single representative radius $R_{\rm sh}$ and (lab-frame) velocity $v_{\rm sh}$. The unshocked CSM is characterized by its solid angle $4\pi f_\Omega$, velocity $v_{\rm CSM} \ll v_{\rm sh}$, and a radial density profile

$$\rho_{\rm CSM} = Ar^{-q}, \tag{C1}$$

respectively. The mass $M_{\rm sh}$ and momentum $M_{\rm sh}v_{\rm sh}$ of the shocked gas increase as the FS and RS sweep up the CSM and SN ejecta, respectively, their evolution obeying

$$\frac{dM_{\rm sh}}{dt} = 4\pi f_\Omega R_{\rm sh}^2 \rho_{\rm SN}(v_{\rm SN} - v_{\rm sh}) + 4\pi f_\Omega R_{\rm sh}^{2-q} A(v_{\rm sh} - v_{\rm CSM}), \tag{C2}$$

$$\frac{d(M_{\rm sh}v_{\rm sh})}{dt} = 4\pi f_\Omega R_{\rm sh}^2 \rho_{\rm SN} v_{\rm SN}(v_{\rm SN} - v_{\rm sh}) + 4\pi f_\Omega R_{\rm sh}^{2-q} A v_{\rm CSM}(v_{\rm sh} - v_{\rm CSM}), \tag{C3}$$

where $\rho_{\rm SN} = M/(4\pi R^2/3)$ is the ejecta density (taken to be a homogeneous sphere of radius R) and $v_{\rm SN} = v(R_{\rm sh}/R)$ its velocity (assuming homologous expansion). Momentum conservation (Equation (C3)) can be rewritten as

$$M_{\rm sh}\frac{dv_{\rm sh}}{dt} = 4\pi f_\Omega R_{\rm sh}^2 \rho_{\rm SN}(v_{\rm SN} - v_{\rm sh})^2 - 4\pi f_\Omega R_{\rm sh}^{2-q} A(v_{\rm sh} - v_{\rm CSM})^2. \tag{C4}$$

The dynamics of the swept-up shell is thus determined by solving Equations (C2) and (C4) with initial conditions $R_{\rm sh} = R_0$, $v_{\rm sh} = 0$, and $M_{\rm sh} \ll M$ for assumed values of A, q, $v_{\rm CSM}$, and f_Ω.

Once the shock dynamics are determined, we estimate the total shock luminosity (ejecta heating rate) as the sum of the kinetic luminosities of the FS and RS shocks, given, respectively, by

$$L_{\rm kin,FS} = 4\pi f_\Omega R_{\rm sh}^2 (v_{\rm sh} - v_{\rm CSM}) e_{\rm FS} = \frac{9\pi}{2} f_\Omega R_{\rm sh}^{2-q} A (v_{\rm sh} - v_{\rm CSM})^3, \tag{C5}$$

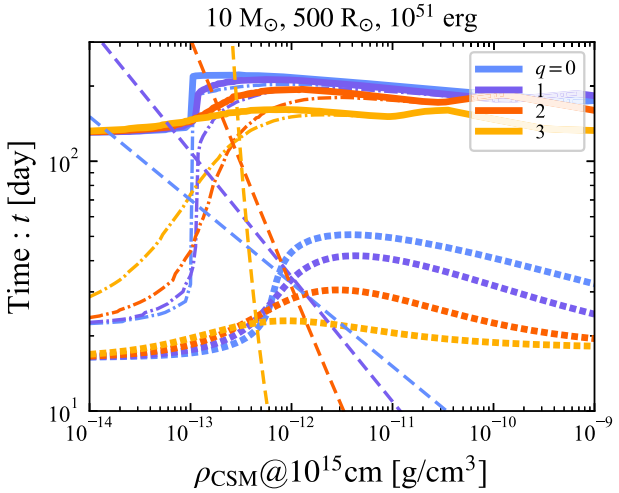

Figure 15. The same as Figure 11 but for different slopes of the CSM radial density profile, $\rho_{\rm CSM} \propto r^{-q}$ (indicated by the different colors). The thick solid lines denote the plateau duration and the dotted lines denote the time at which $T_{\rm eff} = T_{\rm i}$. The dashed diagonal lines denote the shock deceleration timescale. The horizontal axis denotes the CSM density at 10^{15} cm.

$$L_{\rm kin,RS} = 4\pi f_\Omega R_{\rm sh}^2 (v_{\rm SN} - v_{\rm sh}) e_{\rm RS} = \frac{27 f_\Omega M R_{\rm sh}^2 (v_{\rm SN} - v_{\rm sh})^3}{8R^3}, \tag{C6}$$

where the internal energy density of the post-FS (post-RS) region is given by

$$e_{\rm FS(RS)} = \frac{2\rho_{\rm CSM(SN)}(v_{\rm sh} - v_{\rm CSM(SN)})^2}{(\gamma+1)(\gamma-1)}. \tag{C7}$$

Here, γ is the adiabatic index and we adopt $\gamma = 5/3$. In a more detailed calculation, the dynamics of the shocks would be coupled to that of the SN ejecta via heating, such that their evolution should be calculated self-consistently.

Figure 15 shows the key timescales' plot (see Figure 11) as a function of the CSM density normalization at $r = 10^{15}$ cm for different values of the CSM power-law slope q, as marked. The qualitative features in all cases follow those in the standard $q = 2$ wind-like profile. The impacts on the recombination time (thick dashed curves) and the plateau duration (thick solid curves) are slightly larger for smaller q. This may be because for $q < 2$, the shock luminosity increases with time, peaking on the deceleration time.[13] Furthermore, the fact that deceleration starts earlier helps to satisfy the condition of Equation (73) for a longer time. Nonetheless, the plateau duration is not extended more than a few times the zero-heating case ($\rho_{\rm CSM} \to 0$), even for $q \neq 2$.

Appendix D
Glossary of Symbols and Notations

Table 1 summarizes the symbols and notations of characteristic quantities.

[13] An increasing heating rate potentially pushes the photosphere outward during the recombination phase, $dx/dt > 0$. This occurs when the dimensionless photosphere becomes smaller than

$$x_{\rm cr} = \frac{1}{2}\left\{-\left(\frac{t}{t_{\rm diff}}\right)^2 + \sqrt{\left(\frac{t}{t_{\rm diff}}\right)^4 + 8\left(\frac{H}{H_{\rm cr}}\right)}\right\}^{1/2}, \tag{C8}$$

while we confirm that the photosphere always shrinks in our calculations.

Table 1
Definitions of Key Timescales and Heating Rates

Notation	Equation	Meaning
$t_{\rm dyn}$	(3)	Dynamical time
$t_{\rm diff}$	(4)	Diffusion time
$t_{\rm i}$	(28)	Recombination time (beginning of recombination phase)
t_0	(23)	Initial dynamical time
$t_{\rm h}$	(24)	Heating timescale (heating starts to modify thermal evolution)
$t_{\rm h}^{\rm rec}$	(29)	Heating timescale during recombination phase
$t_{\rm diff}^{\rm rec}$	(30)	Diffusion timescale during recombination phase (after which $L \simeq H$)
$t_{\rm pl}$	(33)	Plateau duration (when ejecta becomes optically thin) including heating effects
$t_{\rm thin}$	(34)	When fully ionized ejecta becomes optically thin
$t_{\rm acc}$	(38)	Acceleration timescale (heating source starts to significantly accelerate ejecta)
$t_{\rm diff}^{\rm acc}$	(40)	Diffusion timescale for accelerated ejecta
$t_{\rm i}^{\rm acc}$	(43)	Recombination timescale for accelerated ejecta
$t_{\rm pl}^{\rm acc}$	(44)	Plateau duration for accelerated ejecta
$t_{\rm pl,max}$	(46)/(48)	Maximal plateau duration (Equation (48) if Equation (47) is satisfied)
$t_{\rm pl,Popov}$	(17)	Plateau duration in heating-free case (Popov formulae)
$t_{\rm thin}^{\rm acc}$	(50)	Accelerated fully ionized ejecta becomes optically thin
$t_{\rm br}$	(54)	Break time in broken-power-law heating rate
$H_{\rm cr}$	(12)	Critical heating rate (above which recombination is delayed significantly)
$H_{\rm min}$	(35)	Minimal heating rate that can precisely prolong plateau duration $H = 0$ limit
$H_{\rm pl,max}$	(45)	Heating rate that maximizes plateau duration (Equation (12) if Equation (47) is satisfied)
$H_{\rm thin}$	(49)	Minimal heating rate required to keep ejecta ionized until it becomes optically thin

ORCID iDs

Tatsuya Matsumoto https://orcid.org/0000-0002-9350-6793
Brian D. Metzger https://orcid.org/0000-0002-4670-7509
Jared A. Goldberg https://orcid.org/0000-0003-1012-3031

References

Anderson, J. P. 2019, A&A, 628, A7
Anderson, J. P., González-Gaitán, S., Hamuy, M., et al. 2014, ApJ, 786, 67
Andrews, J. E., Sand, D. J., Valenti, S., et al. 2019, ApJ, 885, 43
Andrews, J. E., & Smith, N. 2018, MNRAS, 477, 74
Andrews, J. E., Smith, N., McCully, C., et al. 2017, MNRAS, 471, 4047
Arcavi, I., Howell, D. A., Kasen, D., et al. 2017, Natur, 551, 210
Arnett, W. D. 1980, ApJ, 237, 541
Arnett, W. D. 1982, ApJ, 253, 785
Barbon, R., Ciatti, F., & Rosino, L. 1979, A&A, 72, 287
Barkat, Z., Rakavy, G., & Sack, N. 1967, PhRvL, 18, 379
Bersten, M. C., Benvenuto, O., & Hamuy, M. 2011, ApJ, 729, 61
Bilinski, C., Smith, N., Williams, G. G., et al. 2020, MNRAS, 498, 3835
Bilinski, C., Smith, N., Williams, G. G., et al. 2024, MNRAS, 529, 1104
Blagorodnova, N., Kotak, R., Polshaw, J., et al. 2017, ApJ, 834, 107
Blondin, J. M., Lundqvist, P., & Chevalier, R. A. 1996, ApJ, 472, 257
Bond, H. E., Henden, A., Levay, Z. G., et al. 2003, Natur, 422, 405
Bostroem, K. A., Valenti, S., Horesh, A., et al. 2019, MNRAS, 485, 5120
Chandrasekhar, S. 1964, ApJ, 140, 417
Chatzopoulos, E., Wheeler, J. C., & Vinko, J. 2012, ApJ, 746, 121
Chen, K.-J., Heger, A., Woosley, S., Almgren, A., & Whalen, D. J. 2014a, ApJ, 792, 44
Chen, K.-J., Heger, A., Woosley, S., et al. 2014b, ApJ, 790, 162
Chen, K.-J., Whalen, D. J., Woosley, S. E., & Zhang, W. 2023, ApJ, 955, 39
Chevalier, R. A. 1989, ApJ, 346, 847
Chugai, N. N. 1991, SvAL, 17, 210
Chugai, N. N., & Danziger, I. J. 1994, MNRAS, 268, 173
Dessart, L. 2018, A&A, 610, L10
Dessart, L., & Audit, E. 2018, A&A, 613, A5
Dessart, L., & Hillier, D. J. 2019, A&A, 625, A9
Dessart, L., Waldman, R., Livne, E., Hillier, D. J., & Blondin, S. 2013, MNRAS, 428, 3227
Dexter, J., & Kasen, D. 2013, ApJ, 772, 30
Falk, S. W., & Arnett, W. D. 1977, ApJS, 33, 515
Faran, T., Goldfriend, T., Nakar, E., & Sari, R. 2019, ApJ, 879, 20
Faran, T., Poznanski, D., Filippenko, A. V., et al. 2014, MNRAS, 442, 844
Fassia, A., Meikle, W. P. S., Vacca, W. D., et al. 2000, MNRAS, 318, 1093
Fransson, C., Ergon, M., Challis, P. J., et al. 2014, ApJ, 797, 118
Fraser, M. 2020, RSOS, 7, 200467
Fuller, G. M., Woosley, S. E., & Weaver, T. A. 1986, ApJ, 307, 675
Gagliano, A., Contardo, G., Foreman-Mackey, D., Malz, A. I., & Aleo, P. D. 2023, ApJ, 954, 6
Gal-Yam, A. 2019, ARA&A, 57, 305
Gezari, S., Halpern, J. P., Grupe, D., et al. 2009, ApJ, 690, 1313
Gilmer, M. S., Kozyreva, A., Hirschi, R., Fröhlich, C., & Yusof, N. 2017, ApJ, 846, 100
Goldberg, J. A., & Bildsten, L. 2020, ApJL, 895, L45
Goldberg, J. A., Bildsten, L., & Paxton, B. 2019, ApJ, 879, 3
Grasberg, E. K., & Nadezhin, D. K. 1976, Ap&SS, 44, 409
Grassberg, E. K., Imshennik, V. S., & Nadyozhin, D. K. 1971, Ap&SS, 10, 28
Hamuy, M. 2003, ApJ, 582, 905
Heger, A., Fryer, C. L., Woosley, S. E., Langer, N., & Hartmann, D. H. 2003, ApJ, 591, 288
Heger, A., & Woosley, S. E. 2002, ApJ, 567, 532
Hiramatsu, D., Matsumoto, T., Berger, E., et al. 2024, ApJ, 964, 181
Inserra, C. 2019, NatAs, 3, 697
Inserra, C., Smartt, S. J., Gall, E. E. E., et al. 2018, MNRAS, 475, 1046
Inserra, C., Turatto, M., Pastorello, A., et al. 2012, MNRAS, 422, 1122
Ivanova, N., Justham, S., Chen, X., et al. 2013, A&ARv, 21, 59
Jeffery, D. J. 1999, arXiv:astro-ph/9907015
Ivezić, Ž., Kahn, S. M., Tyson, J. A., et al. 2019, ApJ, 873, 111
Kangas, T., Fransson, C., Larsson, J., et al. 2022, MNRAS, 511, 2977
Kaplan, N., & Soker, N. 2020, MNRAS, 492, 3013
Kasen, D., & Bildsten, L. 2010, ApJ, 717, 245
Kasen, D., Metzger, B. D., & Bildsten, L. 2016, ApJ, 821, 36
Kasen, D., & Woosley, S. E. 2009, ApJ, 703, 2205
Kasen, D., Woosley, S. E., & Heger, A. 2011, ApJ, 734, 102
Kasliwal, M. M. 2011, PhD thesis, California Institute of Technology
Khatami, D. K., & Kasen, D. N. 2019, ApJ, 878, 56
Khatami, D. K., & Kasen, D. N. 2024, ApJ, 972, 140
Kozyreva, A., Blinnikov, S., Langer, N., & Yoon, S. C. 2014a, A&A, 565, A70
Kozyreva, A., Nakar, E., & Waldman, R. 2019, MNRAS, 483, 1211
Kozyreva, A., Yoon, S. C., & Langer, N. 2014b, A&A, 566, A146
Kurfürst, P., & Krtička, J. 2019, A&A, 625, A24
Kurfürst, P., Pejcha, O., & Krtička, J. 2020, A&A, 642, A214
Leonard, D. C., Filippenko, A. V., Barth, A. J., & Matheson, T. 2000, ApJ, 536, 239
Litvinova, I. I., & Nadezhin, D. K. 1983, Ap&SS, 89, 89
Litvinova, I. Y., & Nadezhin, D. K. 1985, SvAL, 11, 145
LSST Science Collaboration 2009, arXiv:0912.0201
MacLeod, M., & Loeb, A. 2020a, ApJ, 893, 106

MacLeod, M., & Loeb, A. 2020b, ApJ, 895, 29
MacLeod, M., Macias, P., Ramirez-Ruiz, E., et al. 2017, ApJ, 835, 282
Maeda, K., Tanaka, M., Nomoto, K., et al. 2007, ApJ, 666, 1069
Mannucci, F., Della Valle, M., & Panagia, N. 2007, MNRAS, 377, 1229
Martinez, L., Bersten, M. C., Anderson, J. P., et al. 2022a, A&A, 660, A40
Martinez, L., Bersten, M. C., Anderson, J. P., et al. 2022b, A&A, 660, A41
Matsumoto, T., & Metzger, B. D. 2022a, ApJ, 936, 114
Matsumoto, T., & Metzger, B. D. 2022b, ApJ, 938, 5
Matsumoto, T., Nakauchi, D., Ioka, K., Heger, A., & Nakamura, T. 2015, ApJ, 810, 64
Matsumoto, T., Nakauchi, D., Ioka, K., & Nakamura, T. 2016, ApJ, 823, 83
Matzner, C. D. 2003, MNRAS, 345, 575
Mauerhan, J. C., Smith, N., Silverman, J. M., et al. 2013, MNRAS, 431, 2599
McDowell, A. T., Duffell, P. C., & Kasen, D. 2018, ApJ, 856, 29
Metzger, B. D. 2010, MNRAS, 409, 284
Metzger, B. D., Beniamini, P., & Giannios, D. 2018, ApJ, 857, 95
Metzger, B. D., Margalit, B., Kasen, D., & Quataert, E. 2015, MNRAS, 454, 3311
Metzger, B. D., & Pejcha, O. 2017, MNRAS, 471, 3200
Metzger, B. D., Piro, A. L., & Quataert, E. 2008, MNRAS, 390, 781
Michel, F. C. 1988, Natur, 333, 644
Miller, A. A., Chornock, R., Perley, D. A., et al. 2009, ApJ, 690, 1303
Montero, P. J., Janka, H.-T., & Müller, E. 2012, ApJ, 749, 37
Moriya, T. J., Chen, K.-J., Nakajima, K., Tominaga, N., & Blinnikov, S. I. 2021a, MNRAS, 503, 1206
Moriya, T. J., Harikane, Y., & Inoue, A. K. 2023, MNRAS, 526, 2400
Moriya, T. J., Inserra, C., Tanaka, M., et al. 2022, A&A, 666, A157
Moriya, T. J., Jiang, J.-a., Yasuda, N., et al. 2021b, ApJ, 908, 249
Moriya, T. J., Maeda, K., Taddia, F., et al. 2013, MNRAS, 435, 1520
Moriya, T. J., Müller, B., Chan, C., Heger, A., & Blinnikov, S. I. 2019, ApJ, 880, 21
Moriya, T. J., Nicholl, M., & Guillochon, J. 2018, ApJ, 867, 113
Müller, T., Prieto, J. L., Pejcha, O., & Clocchiatti, A. 2017, ApJ, 841, 127
Murphy, J. W., Mabanta, Q., & Dolence, J. C. 2019, MNRAS, 489, 641
Nadyozhin, D. K. 1994, ApJS, 92, 527
Nagao, T., Maeda, K., & Ouchi, R. 2020, MNRAS, 497, 5395
Nagele, C., Umeda, H., Takahashi, K., Yoshida, T., & Sumiyoshi, K. 2020, MNRAS, 496, 1224
Nagele, C., Umeda, H., Takahashi, K., Yoshida, T., & Sumiyoshi, K. 2022, MNRAS, 517, 1584
Nakar, E., Poznanski, D., & Katz, B. 2016, ApJ, 823, 127
Nicholl, M., Blanchard, P. K., Berger, E., et al. 2020, NatAs, 4, 893
Nyholm, A., Sollerman, J., Tartaglia, L., et al. 2020, A&A, 637, A73
Orellana, M., Bersten, M. C., & Moriya, T. J. 2018, A&A, 619, A145
Pejcha, O., Metzger, B. D., & Tomida, K. 2016a, MNRAS, 455, 4351
Pejcha, O., Metzger, B. D., & Tomida, K. 2016b, MNRAS, 461, 2527
Pejcha, O., Metzger, B. D., Tyles, J. G., & Tomida, K. 2017, ApJ, 850, 59
Pejcha, O., & Prieto, J. L. 2015, ApJ, 799, 215
Perley, D. A., Fremling, C., Sollerman, J., et al. 2020, ApJ, 904, 35
Perna, R., Duffell, P., Cantiello, M., & MacFadyen, A. I. 2014, ApJ, 781, 119
Perna, R., Lazzati, D., & Cantiello, M. 2018, ApJ, 859, 48
Popov, D. V. 1993, ApJ, 414, 712
Quataert, E., & Kasen, D. 2012, MNRAS, 419, L1
Rakavy, G., & Shaviv, G. 1967, ApJ, 148, 803
Rose, B. M., Baltay, C., Hounsell, R., et al. 2021, arXiv:2111.03081
Smith, N., Mauerhan, J. C., & Prieto, J. L. 2014, MNRAS, 438, 1191
Smith, N., & McCray, R. 2007, ApJL, 671, L17
Sollerman, J., Taddia, F., Arcavi, I., et al. 2019, A&A, 621, A30
Spitkovsky, A. 2006, ApJL, 648, L51
Strotjohann, N. L., Ofek, E. O., Gal-Yam, A., et al. 2021, ApJ, 907, 99
Strotjohann, N. L., Ofek, E. O., Gal-Yam, A., et al. 2024, ApJ, 960, 72
Subrayan, B. M., Milisavljevic, D., Chornock, R., et al. 2023, ApJL, 948, L19
Sukhbold, T., Ertl, T., Woosley, S. E., Brown, J. M., & Janka, H. T. 2016, ApJ, 821, 38
Sukhbold, T., & Thompson, T. A. 2017, MNRAS, 472, 224
Suzuki, A., & Maeda, K. 2021, ApJ, 908, 217
Suzuki, A., Moriya, T. J., & Takiwaki, T. 2019, ApJ, 887, 249
Swartz, D. A., Sutherland, P. G., & Harkness, R. P. 1995, ApJ, 446, 766
Tsuna, D., Matsumoto, T., Wu, S. C., & Fuller, J. 2024, ApJ, 966, 30
Tylenda, R., Hajduk, M., Kamiński, T., et al. 2011, A&A, 528, A114
Tylenda, R., & Soker, N. 2006, A&A, 451, 223
Uchida, H., Shibata, M., Yoshida, T., Sekiguchi, Y., & Umeda, H. 2017, PhRvD, 96, 083016
Valenti, S., Howell, D. A., Stritzinger, M. D., et al. 2016, MNRAS, 459, 3939
Van Marle, A. J., Smith, N., Owocki, S. P., & Van Veelen, B. 2010, MNRAS, 407, 2305
Vlasis, A., Dessart, L., & Audit, E. 2016, MNRAS, 458, 1253
Vurm, I., & Metzger, B. D. 2021, ApJ, 917, 77
Wang, L.-J., Liu, L.-D., Lin, W.-L., et al. 2022, ApJ, 933, 102
Wiseman, P., Wang, Y., Honig, S., et al. 2023, MNRAS, 522, 3992
Woosley, S. E. 2010, ApJL, 719, L204
Woosley, S. E. 2018, ApJ, 863, 105
Woosley, S. E., Blinnikov, S., & Heger, A. 2007, Natur, 450, 390
Woosley, S. E., & Smith, N. 2022, ApJ, 938, 57
Young, T. R. 2004, ApJ, 617, 1233
Zha, S., Müller, B., Weir, A., & Heger, A. 2023, ApJ, 952, 155